UNIVERSITÀ DEGLI STUDI DI PADOVA

DIPARTIMENTO DI SCIENZE CHIMICHE

CORSO DI LAUREA MAGISTRALE IN SUSTAINABLE CHEMISTRY AND TECHNOLOGIES FOR CIRCULAR ECONOMY

TESI DI LAUREA MAGISTRALE

Sustainable Valorization of Ladle Slag: A Thermodynamic Optimization for Ferrosilicon Production Through an Aluminothermic Reduction

Relatore: Prof. Katya Brunelli

Correlatore: Ing. Maurizio Bellotto

Controrelatore: Prof. Mauro Carraro

Laureando: Mehran Ghadimi Soyeni 2085845

ANNO ACCADEMICO 2024/20

Statement of originality

I, Mehran Ghadimi Soyeni, hereby declare that the work presented in this dissertation, titled "Sustainable Valorization of Ladle Slag: A Thermodynamic Optimization for Ferrosilicon Production Through an Aluminothermic Reduction", is entirely my own original work. I affirm that it has not been fully or partially submitted previously in any other Italian or foreign university for assessment purposes.

I further confirm that the content of this dissertation is the result of my own intellectual endeavours, and I have appropriately cited all sources used. This work does not infringe upon the intellectual property rights of any third party, and its contents do not constitute plagiarism.

I understand the consequences of submitting work that is not my own and affirm the honesty and integrity of this academic contribution.

Mehran Ghadimi Soyeni

Index

Abstract

The iron and steelmaking industries generate significant amounts of slag, a by-product rich in oxides such as iron oxide and silica. Meanwhile, the production of silicon and ferrosilicon is highly energy-intensive and results in substantial emissions. Given the increasing emphasis on sustainability in these sectors, this study explores the valorization of ladle furnace slag through aluminothermic reduction to connect these two industries. The goal is to recover iron and silicon from the slag in the form of ferrosilicon while producing a calcium aluminate-based residual slag suitable for downstream applications, such as high-alumina cement production. To achieve this, thermodynamic modeling and phase-diagram analysis, using the software FactSage, were used to determine the optimal temperatures and chemical ratios for the process. A practical furnace test was then conducted to compare experimental results with theoretical predictions. The simulation confirmed that, under carefully controlled conditions, an iron–silicon alloy can be effectively formed alongside the production of value-added calcium aluminate phases. However, the experiment revealed challenges, such as partial slag fusion and incomplete oxide reduction, suggesting that further process optimization is needed. These findings present a promising approach to reducing the environmental footprint and resource demands of conventional metallurgical processes. Future research should focus on refining furnace control and process design to improve alignment between experimental results and thermodynamic simulations.

1 Introduction

1.1 Foundations of Steelmaking: Materials, Energy, and Emissions

1.1.1 From Iron Ores to Steel: basics of Metallurgy

Approximately 5% of the Earth's crust comprises iron compounds, primarily iron oxides. Iron ore reserves with Fe concentrations ranging from 55% to 60% are typically exploited for economically feasible iron extraction (Ghosh & Chatterjee, 2008). Iron (Fe) in iron ore occurs mainly in two forms: hematite (Fe_2O_3), which corresponds to Fe^{3+}, and magnetite (Fe_3O_4), referring to a combination of Fe^{2+} and Fe^{3+} (Poveromo, 1999). Oxide minerals of various other elements, such as silicon, phosphorus, manganese, and aluminum, are also found in iron ores (Ghosh & Chatterjee, 2008).

The first traces of ironmaking techniques by reducing iron oxide date back to 1500 BC. In modern pyrometallurgical processes, the oxidation state of iron is reduced to zero, Fe^0, by removing oxygen. To make this process viable, the iron ore undergoes treatment with a reagent bearing a higher affinity for oxygen. Carbon (C) in the form of coal, coke, or charcoal is employed in commercial ironmaking since oxygen (O) shows a stronger affinity for C than for Fe under certain conditions. The rules of thermodynamics regulate this process; therefore, in pyrometallurgy, temperature is one of the parameters manipulated to optimize the reduction process (Sundholm et al., 1999).

In the iron and steel industry, iron implies the chemical element in its pure form, as well as the carbon-saturated intermediate (e.g., pig iron) and the final (e.g., cast iron) product. In contrast, the term steel refers to an alloy of iron and carbon, where carbon steel is the most common variety (IEA, 2020).

Steel, with a production of over 1.9 billion tons per year, is the third most commonly used material globally, after cement and timber. Due to its low cost, high strength, recyclability, durability, and workability, steel is an essential component in various sectors, including construction, transportation, infrastructure, machinery, and consumer goods (IEA, 2020).

There are over 3,500 varieties of steel, produced by adding different alloying elements such as molybdenum, vanadium, manganese, tungsten, and titanium to create a set of desired characteristics or modify the already existing ones to meet the requirements of the ultimate application. For instance, stainless steel, formed by mixing chromium

and nickel, is an attractive choice for cookware due to its corrosion resistance. Steel's properties can be influenced by modifications to its carbon content[1]. Generally, carbon steel typically contains less than 0.25% carbon; however, some may contain up to 2% (World Steel Association, 2018).

1.1.2 From Energy Consumption to Clean Transition

Steel production heavily depends on energy, and the energy system requires steel as a raw material. The ferromagnetic characteristics of steel and its alloys impact energy generation and use, making steel a key material for the transition to clean energy sources. Steel is essential component to many significant energy-producing infrastructures[2], such as nuclear power plants, wind turbines, transmission and distribution networks, and hydropower plants (IEA, 2020).

Although steel promotes clean energy, its heavy reliance on coal and coke as fuels and reduction agents adds to the current climate crisis. The industry contributes 25% of industrial CO_2 emissions, or 2.6 gigatons of carbon dioxide annually, making up 7 to 9% of the total CO_2 emissions worldwide (Babich & Senk, 2013). The production of iron and steel accounts for approximately 20 percent of industrial energy consumption and roughly 8% of total energy use globally, placing it among the most energy-intensive production activities (Brown et al., 2012).

1.2 Steel Production Pathways: A Technological Overview

1.2.1 Inputs and Foundations of Modern Steel Production

Although some artifacts of iron and steel are 5,000 years old, large-scale manufacturing only became possible during the Industrial Revolution of the 18th and 19th centuries. Iron ore, steel scrap, lime fluxes (namely limestone and dolomite), energy (mainly coal, natural gas, and electricity), and reducing agents (mostly carbon-based) are the main inputs to steelmaking today (Figure 1). While iron ore and scrap supply the metallic charge, with scrap having a higher metallic content (>95%) than

[1] Rising steel carbon content increases hardness (resistance to scratch) and brittleness (tendency to fracture rather than bend under force). High-carbon steels, such as tools, are commonly used for applications requiring abrasion resistance. However, a more desirable quality in steel is its ductility (opposite of brittleness). Steel's ability to deform elastically and plastically without breaking makes it ideal for structural applications like building beams, columns, and vehicle chassis (IEA, 2020).

[2] The availability of large amounts of plastic, particularly since the middle of the twentieth century, has resulted in the displacement of steel in some applications, such as specific components of buildings (e.g., pipes and fittings) and automobiles (e.g., bumpers and external body panels) (IEA, 2020).

iron ore (50-70%), energy inputs heat the metallic input and chemically reduce iron ore. Coke, used as a reducing agent, is made by the transformation of coal by a process called coking. This process entails treating a specific grade of coal named hard coal, which has higher carbon content, under anaerobic conditions at elevated temperatures to remove volatile components. Lime fluxes are applied at multiple stages of the steelmaking process to eliminate impurities such as sulfur, phosphorus, and silica, the removal of which results in CO_2 emissions. When chemically coupled with the non-iron constituents of iron ore, these impurities generate a steelmaking co-product known as slag (IEA, 2020; Remus et al., 2013).

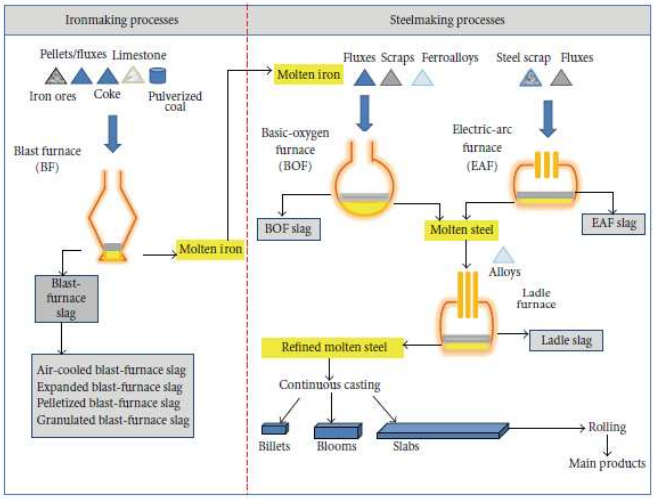

Figure 1 Schematic representation of Iron and steelmaking inputs and outputs(Yildirim & Prezzi, 2011).

1.2.2 Understanding the Steelmaking Routes and Stages

Overall, there are two main routes of steelmaking in the world: 'primary' steel production, which uses iron ore as its main source of metallic input, whereas 'secondary' production relies on scrap[3]. The production of crude steel involves three stages: raw material processing, ironmaking, and steelmaking.

The quality of the raw material affects the efficiency of the iron and steelmaking stages by determining the amount of coke, natural gas, and electricity used. Therefore, iron ores go through a series of processing stages to ensure a high quality of raw material feed. For instance, iron ore fines are agglomerated by treating with heat and pressure

[3] Nevertheless, this distinction has become less obvious in many cases, as scarp is employed in primary production and iron is frequently used in electric furnaces, which are the standard unit of secondary production (IEA, 2020).

to produce nodules (sinter) or pebble-sized particles (pellets) to ensure the flow of gas within the furnace (IEA, 2020; Remus et al., 2013).

According to a study carried out by Mousa et al. (2016), iron and Steelmaking stages can be divided into four primary routes: blast furnace/basic oxygen furnace (BF-BOF), direct reduction/electric arc furnace (DRI-EAF), smelting reduction/basic oxygen furnace (SR-BOF), and scrap melting in an electric arc furnace (EAF). A clear distinction of these pathways is displayed in Figure 2.

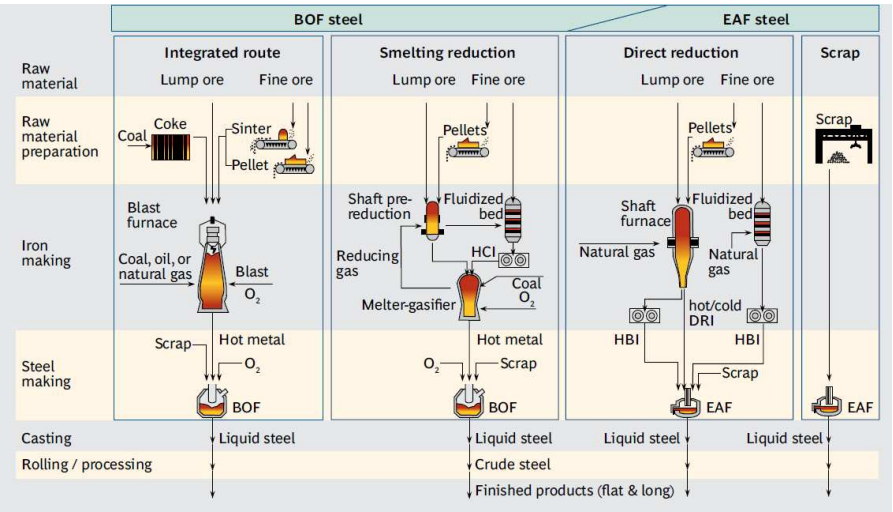

Figure 2 Graphical representation of steelmaking routes with raw material inputs, processes, and outputs (Wörtler et al., 2013).

1.2.3 The BF-BOF Pathway: Backbone of Primary Steelmaking

The most common primary production pathway is the blast furnace-basic oxygen furnace (BF-BOF) route, accounting for around 70 percent of global steel production and roughly 90 percent of primary route steel production. Coke and iron ore are fed into the blast furnace from the top. Concurrently, hot air and pulverized coal or natural gas are introduced through pipelines located on the side of the lower section of the furnace, known as the tuyeres (Figure 3). This creates a counter-current process, where descending iron ore meets rising reducing gases. The blast furnace also uses additives, such as lime fluxes, in varying quantities to control temperature and impurity levels. The blast furnace generates molten iron, referred to as hot metal (the main input to basic oxygen furnace) at temperatures ranging from 1,400 to 1,500°C. The final energy input required to produce one ton of liquid steel using the BF-BOF pathway is approximately 15 GJ (IEA, 2020).

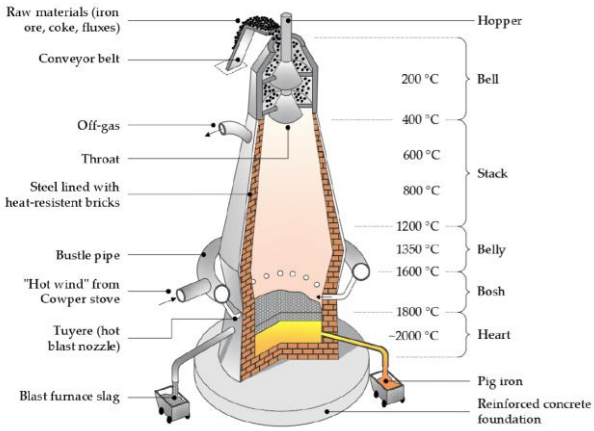

Figure 3 Schematic illustration of blast furnace, internal parts, and temperature gradients (Piemonti et al., 2021).

The BOF[4] is used to lower the carbon content from approximately 4–5% to the level needed for the steel grade (usually about 0.25%)[5]. This is achieved by injecting supersonic oxygen vertically through a lance with numerous holes onto molten hot metal in a cylindrical converter (Figure 4). In addition to reducing carbon content, this process also removes unwanted elements by reacting impurities with burnt lime or dolomite, which forms the steel slag. The slag generated during the steelmaking process floats to the surface of the molten steel. Tilting the furnace in one direction allows the slag to be tapped into ladles (Yildirim & Prezzi, 2011; Brandt & Warner, 2005).

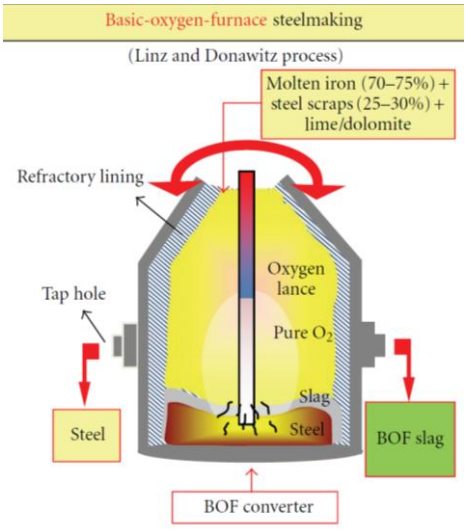

Figure 4 Schematic representation of BOF (Yildirim & Prezzi, 2011).

[4] Because of the process's simplicity and versatility in creating high-quality steels, BOF steelmaking quickly replaced the previously used open hearth furnaces. Instead of the 6-8 hours needed in open hearth furnaces, the new technology could produce steel with the necessary carbon content in just 60 minutes (Ghosh & Chatterjee, 2008).

[5] The BOF process is autothermal, meaning it generates its own thermal energy from carbon oxidation and other impurities in heated metal (mainly silicon and phosphorus) (Piemonti et al., 2021).

1.2.4 The SR-BOF Pathway: An Integrated Steelmaking Alternative

The smelting reduction converter (SR-BOF) path is an alternative process for the production of steel, replacing the traditional BF-BOF route with a two-stage process. The first step involves pre-reducing iron ores. Depending on the type of iron ore, the furnace used in this stage varies: a shaft furnace is used in Corex technology for treating pellets and fines, while a multistage fluidized bed reactor processes fine ore in Finex technology. The second stage melts the pre-reduced iron ores in a furnace called a melter-gasifier using coal and pure oxygen to transform iron into hot metal, while removing undesirable components (gangue) in the form of liquid slag from iron ores and coal ash. The melter-gasifier's off-gases, generated during this process, are recirculated and reused for pre-reducing iron ores in the first step (Wörtler et al., 2013).

1.2.5 DRI-EAF Steelmaking: Solid-State Iron Reduction

According to Wörtler et al. (2013), another method for producing iron and steel is the direct reduced iron-electric arc furnace (DRI-EAF) technique. The iron ores remain solid during the process, unlike in BF and SR (smelting reduction). Oxygen is removed through a chemical process with a hot reducing gas, often from natural gas, containing high H_2 and CO content.

The resulting hot DRI can be fed directly to the EAF or compacted into hot briquetted iron (HBI) for improved storage and transport of pyrophoric material. In contrast to hot metal, DRI still has certain amounts of O_2 and other unwanted substances (gangue) that must be separated throughout the steelmaking process. While blast furnace methods still offer the highest yield, the DRI-EAF route has been gaining attention in steel production due to better thermal control in EAF, enabling oxygen potential management and producing cleaner steel by preserving higher percentages of alloying elements (González et al., 2021; Henriques et al., 2023).

1.2.6 The EAF Pathway: From Scrap to Steel

The secondary production path involves collecting and sorting scrap[6], then using electricity instead of gaseous fuel to melt the steel in an electric furnace (Ghosh & Chatterjee, 2008).

[6] Furthermore, in addition to steel scrap, secondary materials in smaller quantities (first, pig iron and CaO in the form of burnt lime or dolomite; then, oxygen and carbon powder) and coal or natural gas(to form a protective slag foam) is charged to furnace as well (Yildirim & Prezzi, 2011).

The Electric Arc Furnace (EAF) produces great heat by generating high-voltage electric arcs between the conductive graphite electrodes and the metal charge, melting the scrap steel or direct reduced iron (DRI) inside the furnace[7] (Figure 5). Burnt lime or dolomite (CaO) is added to the furnace along with the metallic charge or during the melting process. In the steel refining process, oxygen is introduced into the molten steel using an oxygen lance. Oxygen injections oxidize iron, aluminum, silicon, manganese, phosphorus, and carbon in heated metal. These oxidized components, when combined with lime (CaO), result in the formation of slag (Yildirim & Prezzi, 2011).

For secondary steel production, Electric arc furnaces (EAFs) are the most popular; however, India and China implement less energy-efficient induction furnaces. Around 2 GJ of final energy is needed to produce one ton of basic steel from scrap[8] (IEA, 2020).

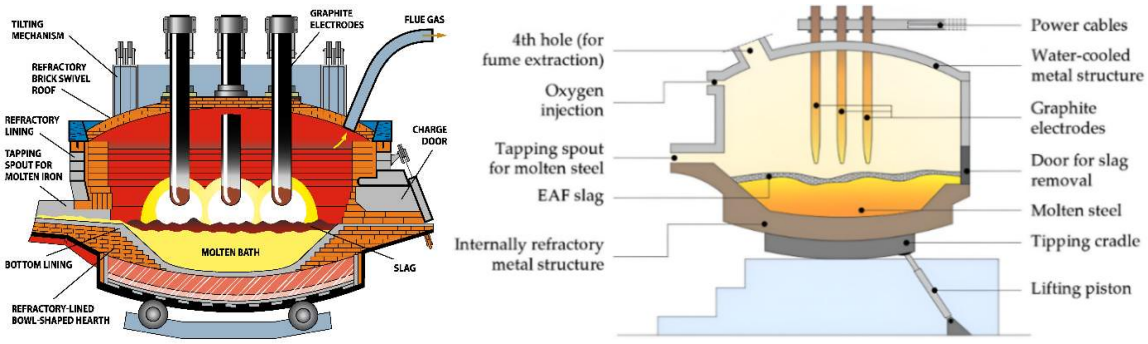

Figure 5 Graphical representations of different parts of EAF (Tomažič et al., 2024) on left and (Piemonti et al., 2021) on right.

1.2.7 Secondary Steelmaking: Refining Molten Steel in the Ladle Furnace

To achieve precise control over chemistry and performance, molten steel tapped from furnaces undergoes additional processing in the ladle. This process of refining steel is called secondary steelmaking, as opposed to primary steelmaking, which takes place in BOFs, EAFs, etc., where the steel is initially produced. The demand for high-quality

[7] The quality, density, and size of the charged materials must be carefully selected for two reasons: the melting and temperature conditions inside the furnace, as well as the chemical composition of the produced steel, must all fall within the required ranges (Yildirim & Prezzi, 2011).

[8] The problem of scrap availability—both in terms of quantity and quality—was brought by EAFs when the focus on production efficiencies led to a drop in scrap generation. At this point, EAFs began using hot metal, DRI, and other scrap alternatives. It also made EAFs capable of reaching the high standards of final steel composition about the concentration of hazardous metals like copper, chromium, nickel, tin, etc., and made EAF steelmaking less dependent on the volatility of scrap supply (IEA, 2020).

steel has led to the adoption of downstream steel processing to ensure the final product's quality (Ghosh & Chatterjee, 2008).

Secondary steelmaking is responsible for reducing the concentration of carbon and dissolved gases in liquid steel, such as oxygen, nitrogen, and hydrogen, along with sulfur. All of these significantly impact steel performance in terms of ductility, impact strength, and corrosion resistance by occupying interstitial sites in the iron lattice (Yildirim & Prezzi, 2011; Ghosh & Chatterjee, 2008).

The most common unit in secondary steelmaking is the ladle furnace. The ladle holding the liquid steel is carried to the LF station, where it is sealed with a lid, and graphite electrodes are placed inside. Additives are used in the LF to deoxidize and modify the composition of the melt, while arc heating controls the temperature. Sulfur content in steel can be reduced to 0.0002% by injecting desulfurizing chemicals (e.g., calcium, magnesium, silicon, calcium chloride) through a lance (Remus et al., 2013). As shown in Figure 6, argon is purged from the bottom to stir the bath, while the top cover provides strong protection against atmospheric oxidation. However, since it is not entirely airtight, some air infiltration is inevitable (Ghosh & Chatterjee, 2008).

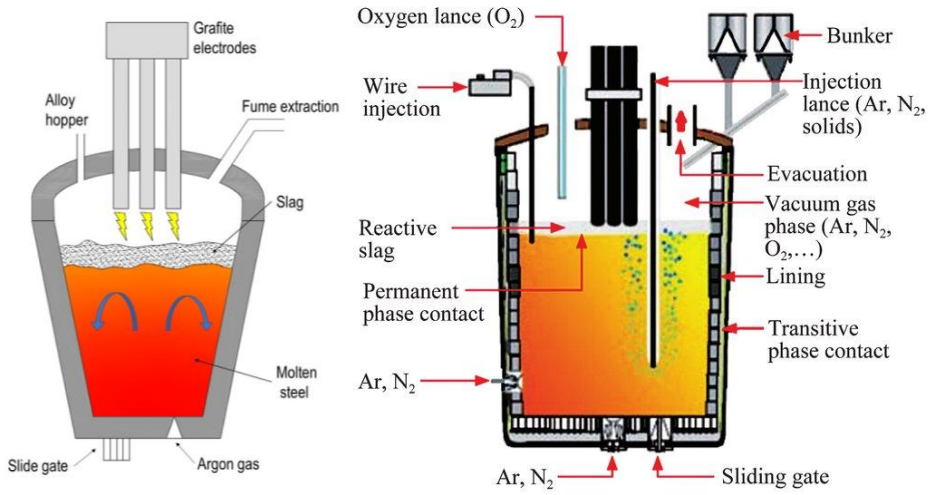

Figure 6 Schematic illustration of LF (Levi at al., 2021) (left); a more detailed look of the internal parts (Guo et al., 2021) (right)

1.3 Composition, Characteristics, and Production of Steelmaking Slags

Based on the research conducted by Piemonti et al. (2021), each production pathway has a different slag-to-steel output ratio: 250–300 kg of blast furnace slag per ton of pig iron produced, 120–180 kg of basic oxygen furnace and electric arc furnace slag

per ton of steel produced, and 30–80 kg of ladle furnace slag per ton of secondary metallurgy-treated steel.

Table 1 presents the typical chemical composition of slags from various steelmaking furnaces.

Reference	Slag type	CaO (%)	Fe_2O_3 (%)	SiO_2 (%)	FeO (%)	Al_2O_3 (%)	MgO (%)	MnO (%)	P_2O_5 (%)
Shi, 2004	BOF	30–55	–	8–20	10–35	1–6	5–15	2–8	–
Yildirim & Prezzi, 2011	BOF	30–60	3–38	7–18	7–35	0.5–4	0.4–14	0.3–4.3	0.2–5
Shi, 2004	EAF	35–60	–	9–32	1–30	2–9	5–15	1–8	–
Yildirim & Prezzi, 2001	EAF	22–60	20–33	6–34	10–40	3–14	3–13	2.5–8	0–1.2

Table 1 Slag composition breakdown according to different literatures.

1.3.1 The Main Steel Slag: BOF slag

As Yildirim & Prezzi (2011) stated, the main chemical components of basic oxygen furnace (BOF) slag are calcium oxide (CaO), iron(II) oxide (FeO)[9], and silicon dioxide (SiO_2). The concentration of silica (SiO_2) in BOF slag varies between 7% and 18%, and the quantities of Al_2O_3 and MgO range from 0.5% to 4% and 0.4% to 14%, respectively. The free lime content may reach up to 12%. Large quantities of lime or dolomitic lime are used in the conversion of iron to steel, resulting in a high CaO content in BOF slag (CaO >35%) (Juckes, 2003; Shi, 2004; Remus et al., 2013).

1.3.2 EAF Slag Composition

In terms of chemical composition, EAF slag is quite similar to BOF slag, but visually, it has a darker color. The Electric Arc Furnace (EAF) steelmaking process mainly involves the recycling of steel scrap. Thus, the chemical composition of EAF slag is strongly influenced by the characteristics of the steel scrap. This explains the fluctuations in the fraction of each component, with FeO, CaO, SiO_2, Al_2O_3, and MgO ranging from 10–40%, 22–60%, 6–34%, 3–14%, and 3–13%, respectively. Nevertheless, the FeO concentration in EAF slag produced during stainless steel manufacturing can be as low as 2%. In addition to solid solutions of CaO, FeO, and

[9] During the transformation of molten iron into steel, depending on the efficiency of the furnace, some of the iron (Fe) in the hot metal is lost and cannot be collected in the finished steel. A slag composition with iron oxide content as high as 38% was found in this regard (Shen et al., 2009).

MgO, EAF slag also contains free CaO and MgO, as well as other complex minerals (Yildirim & Prezzi, 2011). Figure 7 displays the visual appearance of EAF slag generated in a steel plant.

Figure 7 EAF slag generated in a steel plant.

1.3.3 Ladle Furnace slag

The chemical composition of ladle slags (LS) is not well documented in the literature. The steel refining process involves feeding various alloying elements into the ladle furnace to obtain the desired steel grade. As a result, the sought steel grade greatly affects the chemical make-up of ladle slag. In comparison with BOF and EAF slags, ladle slags show a broader chemical composition.

In general, ladle slag exhibits a lower FeO proportion (<10%) than EAF and BOF slags. However, ladle slags often have higher Al_2O_3 and CaO concentrations (Yildirim & Prezzi, 2011). The ladle furnace slag may include slag from the converter or EAF during tapping, deoxidation products, ladle lining wear, residual ladle slag from previous heats, and added slag-forming agents. To produce high-quality steel, top slag composition with high sulfide capacity, inclusion absorption capacity, optimal viscosity, optimal CaO/Al_2O_3 ratio, minimal amount of reducible oxides (FeO + MnO), and the right wetting qualities are necessary (Lachmund et al., 2001).

1.4 Unlocking the Potential of Steel Slag for Sustainable Development

In September 2015, 193 countries adopted the 17 Sustainable Development Goals (SDGs), which aim to 'satisfy the needs of the present without compromising the ability

of future generations to meet their own needs'. The three global challenges that these goals aim to address by 2030 are environmental degradation, severe poverty, and social inequality and injustice. Environmental goals, in particular, include more efficient resource production and consumption, a reduction in waste output, the avoidance and reduction of sea pollution, and action against desertification and deforestation (United Nations, 2024).

The road industry may hinder meeting global environmental targets. This is linked to the use of energy (electricity and fuels) and the consumption of raw materials. One kilometer of new road requires 30,000 tons of stones and 90 tons of bitumen, both of which have significant negative effects on the environment (UEPG, 2017).

To make asphalt mixtures in a more sustainable way, the material circularity concept suggests using waste or by-products as aggregates or fillers, or even as a partial replacement for these materials. Incorporating waste materials into asphalt mixtures reduces the use of natural resources, lowering the carbon footprint and environmental impact resulting from the disposal of these by-products, such as landfilling (Choudhary et al., 2020).

1.4.1 Steel Slag in Roads and Pavements: A Sustainable Infrastructure Solution

In this context, steel slag, a by-product of the steelmaking process that forms during the removal of impurities in iron and steelmaking, has been widely studied for the possibility of its incorporation into road construction.

Based on a study by Chen and Wei (2016) on integrating BOF slag into asphalt mixtures, the following conclusions were drawn. The criteria set by highway agencies for road construction aggregate could be fulfilled by BOF slag Using steel slag as a coarse aggregate alternative can improve the engineering properties of asphalt mixtures. For instance, the angular and abrasive nature of steel slag particles enhances interlocking. Asphalt mixtures including steel slag had better resistance to moisture than asphalt mixtures containing natural aggregate, as demonstrated by the tensile strength ratio Compared to the conventional mixture, the slag mixture exhibited better rutting resistance. Furthermore, ride quality and skid resistance were superior in the sample containing steel slag. The field study showed that steel slag can be used as coarse aggregate in areas with heavy traffic braking or turning.

Regarding EAF slag, Pasetto and Baldo (2011) stated that EAF steel slag is chemically and environmentally compatible with road surface bitumen and has physical and mechanical properties similar to natural aggregates. EAF slag-based asphalt mixtures exhibit good Marshall Stability and Marshall Quotient without sacrificing densification or workability. The mixes also meet the demanding Superpave volumetric requirements during gyratory compaction evaluation, and tests show limited axial distortion, lowering the danger of permanent deformation. The mixture's high stiffness and fatigue resistance have been confirmed by dynamic analyses conducted under slow-channeled traffic circumstances. Additionally, minimal water damage vulnerability indicates durability. The mix with 90% EAF slag performed the best out of all the combinations tested, while mixes containing 60%, 30%, and 0% all showed progressively worse performance. These results highlight the improved mechanical and durability features related to greater slag content.

In another experiment by Kavussi and Qazizadeh (2014) on EAF slag, slag pebbles were found to have a rougher, more angular structure than limestone. Thus, adding more slag to asphalt mixes enhances Marshall Stability and Quotient. SEM analysis shows the porous characteristics of slag, which improve asphalt adhesion and strengthen the aggregate-asphalt bond. By enhancing particle interlocking and internal friction, EAF slag significantly extends fatigue life, according to fatigue testing. Asphalt and slag make a firm bond that slows the formation and spread of cracks. Higher slag ratios restrict aggregate mobility and enhance fatigue resistance.

In terms of the environmental impact, Maghool et al. (2016) concluded that both EAF slag (EAFS) and LF slag (LFS) are classified as inert solid wastes according to environmental tests based on the EPA Victoria Industrial Waste Resource Guideline. They show no leaching or heavy metal contamination and fall within the limits for drinking water standards. Moreover, engineering tests confirm that both slags have low organic content, high density, and durability, making them high-quality aggregates. LFS offers better performance with higher CBR values due to greater particle cohesion and compaction, making it suitable for pavement bases, subbases, and engineering fills. EAFS, on the other hand, is less suitable for base layers due to its lack of cohesiveness and lower CBR values. However, it can be combined with other materials to enhance its properties and be utilized in pavement subbases and engineered fills.

1.4.2 Steel Slags into Building Materials: Toward Circular Construction

According to Abukersh and Fairfield (2011), the typical mass composition of concrete is 10–20% cement, 70–80% natural aggregate (NA), and 5–10% water. Natural resource depletion concerns are rising due to the high demand for concrete, which leads to the overexploitation of high-quality river sand and gravel. To make the situation worse, these resources are often unevenly distributed, causing a supply and demand imbalance in the concrete and cement industry. To ensure sustainable development, the concrete sector must discover alternatives to NAs. Using steel slag might create a sustainable link between the concrete and steel industries. Steel slag's mineral phases consist of C_2S, C_3S, C_4AF, and C_3A, which are similar to Portland cement's mineral phases. This may indicate that steel slags could be used as hydraulic materials. One recycling method is to grind steel slags into a fine powder and utilize it as a cementitious material (Ren & Li, 2023).

A comparison of cement mortar mixtures containing basic oxygen furnace carbon slag (BOF C) and electric arc furnace stainless steel slag (EAF S), as well as their characteristics—such as water demand, setting time, and the effects of slag replacement ratios on cement paste and mortar fluidity—was investigated by Saly et al. (2018). Pure BOF C paste presented a flash set owing to its high aluminate concentration and missing gypsum. Once the BOF C replacement ratio in blended cement paste was increased to 45%, the setting time was decreased while the opposite phenomenon was observed for EAF S, with a prolonged setting time BOF C cement mortar at 15%, 30%, and 45% replacement ratios showed greater compressive strength than EAF S mortar at the same ratios at all ages due to its higher hydraulic phase content, greater alkalinity, and higher pH value. Although the pH values of blended cement containing 50% BOF C or EAF S were lower than those of pure cement, they remained above the key pH threshold required to maintain the passivation coating on steel bars, making them acceptable for protecting steel bars against corrosion in harsh marine conditions.

A series of mechanical behavior of electric arc furnace (EAF) and granulated blast furnace slag (GBF) concretes were examined by Lee et al. (2019). Fresh concrete parameters, such as slump and air content, were tested, finding that mixtures including EAF slag had lower slump and air content than Ordinary Portland Cement (OPC), most likely due to EAF slag's finer particle size. However, the GBF slag concrete acted same

as an OPC. EAF and GBF slag in cement substitutes delayed initial and final setting times, although gypsum slightly shortened them. Both slag concretes showed more autogenous shrinkage than OPC, with EAF shrinkage curves stabilizing after 20 days and GBF after 30 days. Strength measurements at 3, 7, and 28 days revealed that slag concretes acquired strength more slowly than OPC at early ages. However, the addition of gypsum increased the development of strength.

A few years later, Ren and Li (2023) reported that replacing natural aggregate with steel slag aggregate enhances concrete density, making it an ideal nuclear radiation shielding material. Replacing 100% of river sand or gravel with steel slag aggregate reduced slump by 75% or 100%. Coarse steel slag aggregate can fully replace natural aggregate, while fine slag aggregate should not replace more than half of the fine aggregate due to workability concerns. Well-designed steel slag aggregate concretes generally beat natural aggregate concrete in compressive, flexural, and split tensile strength by 50%, 60%, and 60%, respectively. The incorporation of SSA in concrete has the potential to significantly contribute to sustainable development, environmental protection, and economic benefits. For reference, the total lifecycle costs were lower for SSAC, and the cost of SSA compared to NA was 20% lower.

1.4.3 Steel Slag in Metallurgy: Recycling for Resource Efficiency

Regarding steel slag valorization in metallurgical sectors, Chandel et al. (2023) reported that steel slag contains valuable metals and non-metals such as Fe, Ni, Mg, Al, Si, P, and Ti, with minor amounts of V and Ti. The suggested recycling technique for Fe, P_2/P_4, and Mg was reduction using a reducing agent. Furthermore, mechanical separation, exploiting the ferromagnetic properties of certain elements, is an appropriate procedure for iron and zinc recovery. The selective acid leaching technique can recover elements like V, Si, Mg, and Cr; however, the process requires recycling the acidic solvent to minimize environmental impact.

1.5 Silicon and Ferrosilicon: Production and Sustainable Pathways

1.5.1 Fundamentals of Silicon and Ferrosilicon Production Processes

After oxygen, silicon is the second most abundant element in the Earth's crust. Silicon naturally occurs in oxygen-containing compounds, such as silicates and silicon dioxide, which are relatively pure (Schei et al., 1998). Elemental silicon is often

referred to as 'silicon metal', despite being a metalloid rather than a true metal (Kero et al., 2016).

According to a study by Kero et al. (2016), primary silicon manufacturing uses the submerged arc furnace (SAF). Quartz is the main raw material for silicon production, along with reducing agents such as coal, charcoal, wood chips, and coke. Iron pellets or sinter are occasionally added to produce ferrosilicon (Figure 8). Carbon electrodes (pre-baked electrodes for MG-Si and Søderberg electrodes for ferrosilicon) and carbonaceous materials are continuously consumed to produce FeSi and MG-Si[10]. The FeSi production process involves the reduction of iron oxides to metallic iron through reactions with carbon monoxide gas and volatile hydrocarbons (Table 2).

Type of alloy	Generic emission factor
Ferrosilicon 45% Si	2.5
Ferrosilicon 65% Si	3.6
Ferrosilicon 75% Si	4
Ferrosilicon 90% Si	4.8
MG-Si (>98% Si)	5

Table 2 Generic Co_2 emission factor for Si and FeSi alloys (ton Co_2 / ton tapped metal)((Kero et al., 2022).

1.5.2 Sustainability Trends in Silicon and Ferrosilicon Manufacturing

There is interest in decarbonizing the silicon sector. This is challenging due to the intrinsic stability of SiO_2 and the effectiveness of carbon as a reductant (Kero et al., 2022). However, recent developments aim to reduce carbon emissions from traditional SAFs.

[10] Metallurgical grade silicon can be considered as a final or an intermediate stage in Si manufacturing, depending on the purpose. MG-Si is usually used as an alloying agent but when it is intended to be used in solar and electronic applications, Siemens method is frequently utilized to reach the high purity standards required by those uses, resulting in additional emissions around 100kWh/kg Si (Hoover et al., 2024).

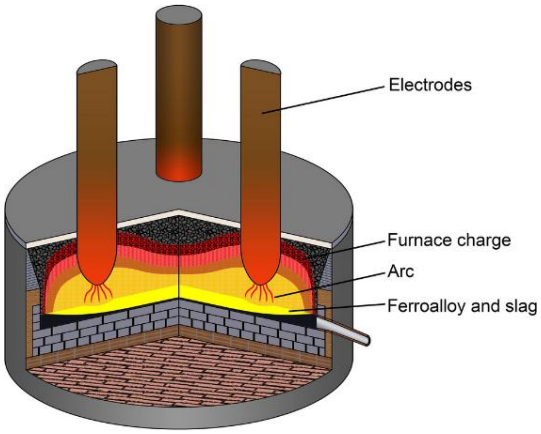

Figure 8 A schematic illustration of submerged arc furnace (Yu et al., 2021).

Elkem's Limpio factory in Paraguay exhibits sustainable ferrosilicon manufacturing via a nearly carbon-neutral process using an 11.5-MW Submerged Arc Furnace (SAF). Locally mined quartz is used as raw material, as well as bio-based carbon material, specifically charcoal, that is obtained from on-site cultivated eucalyptus trees to avoid deforestation of neighboring forests. The plant is completely powered by regional hydroelectric electricity, which further reduces its carbon footprint. This factory exemplifies the circular economy; however, electrode usage emissions and production scalability remain challenges (Elkem, 2018).

Liu et al. (2018) used a submerged arc furnace to produce silicon by replacing a portion of fossil-based reducing agents with alternative carbon materials obtained from pyrolysis of vegetative plant waste with a fixed carbon content of 78.5 wt.%. The study examined three batches. The batch that replaced 20% of fossil reducing agents (coal and petroleum coke) with carbon from waste showed a reduction in CO_2 emissions of 0.817–0.865 ton per ton of silicon. Moreover, the energy consumption (13.81 MWh/t) was close to that of the reference batches, and it achieved the highest yield of 94.5%, surpassing the maximum yield of 86% in the reference cases. Additionally, the carbon efficiency indicator increased from 0.447 and 0.446 in the reference trials to 0.45 in the batch using waste carbon material. The results indicate that integrating treated vegetative waste into an industrial process does not negatively impact technical performance metrics and, in some cases, may even enhance them.

Monsen et al. (2001) produced ferrosilicon using Brazilian charcoal in a 150-kW pilot-scale submerged arc furnace, achieving a metal yield of 89.3%, which was similar to industrial values and 7% higher than the trial using English gas coke. The higher SiO-reactivity with charcoal compared to coke was a key factor in the increased yield. While

the 10 kWh/kg FeSi of electricity consumed to make charcoal was 2 kWh/kg less than that of English gas coke, it was still 2 kWh/kg higher than industrial trials. This study also found that incorporating Brazilian or European charcoal resulted in purer silicon products (99.0% and 98.7%) compared to the reference coke silicon (95.9%), due to the reduced ash content in the charcoal sample.

Nevertheless, SAF operations still face challenges when using 100% biocarbon. Charcoal, for instance, has low mechanical strength and generates fines that may hinder gas flow. Furnace design alterations, along with densifying and heating charcoal feedstocks, have been studied to overcome this issue (Kaffash et al., 2021). Implementing Carbon Capture Utilization and Storage (CCU/CCS) in silicon-making processes is challenging due to the low CO_2 concentration in off-gas. Specifically, about 3–4% of furnace off-gas contains CO_2, while the rest comprises nitrogen, oxygen, water, nitrogen oxides, SO_x, and heavy metals (Nygard et al., 2019). For this reason, the costs make the justifying of this action difficult. In a study by Andersen (2023), it was suggested that recirculating exhaust gas can boost CO_2 concentrations for CCS capabilities. The method involves cooling and filtering exhaust gas before recirculating it to the furnace, which substitutes some of the new air that would otherwise enter the system. Pilot-scale Si furnaces tested this theory and showed an increased CO_2 concentration above 20 vol%. This recirculation also reduced nitrogen oxide emissions, another major pollutant. While this study demonstrated an improved CO_2 concentration and lower carbon capture costs in a pilot-scale furnace, further research is needed to assess industrial applicability.

Another study by Nygård et al. (2019) explored the technical and financial feasibility of applying the CCMS process to capture CO_2 during metallurgical ferrosilicon (FeSi) production. Carbon Capture in Molten Salts (CCMS) traps CO_2 from various sectors such as energy generating and energy-intensive industry flue emissions. The traditional chemical mechanism is based on a calcium looping process in solid state (using CaO-based solid sorbents), in which CO_2 is collected in a carbonation reaction to generate $CaCO_3$, followed by a reverse calcination reaction in a second stage. The novel feature of CCMS is liquid operation in CaO-rich molten salts where the melt repeatedly dissolves $CaCO_3$, leaving highly reactive CaO available for following CO_2. Nygard et al. (2019) conducted an evaluation on a modular plant on one of Elkem's existing 40 MW FeSi furnaces by implementing CCMS method for recycling the flue gas. Assuming a CO_2 capture rate of 85% and compressing it to 70 bar (20°C) results

in a capture cost of 60 EUR/ton, making CCMS a promising alternative for full-scale FeSi production. However, concerns persist regarding the additional heating required and leaks from the heat pipe of the fluidized bed due to corrosion.

Carbon materials such as coal, semi-coke, charcoal, and wood chips were used as reductants in submerged electric arc furnaces for the carbothermal reduction of silica and iron oxide to produce ferrosilicon. Various mixtures of the aforementioned carbon-containing materials were tested to optimize energy consumption and metallurgical performance. The optimal mix consisted of 65% coal, 30% semi-coke, 5% charcoal, and wood chips. Using this combination, the lowest energy consumption (8.46 MWh/ton) was achieved, along with an appropriate silicon recovery rate (93.68%) and a silicon content of 73.58%. By studying the process's thermodynamics and kinetics, as well as raw material characterization, the study concludes that this optimized carbon material combination improves energy efficiency and Si recovery, making it the most effective for ferrosilicon synthesis (Etemadi et al., 2023).

1.6 Metallothermic Reduction: Processes and Sustainable Applications

1.6.1 Metallothermic Reduction: An Overview of Pathways and Potential

Metallothermic reactions, a method long used by alchemists, involve reducing oxides or halides with metals to produce metals and alloys. The general equation for these reactions is:

$$AX + B \rightarrow A + BX$$

where X represents oxygen, chlorine, or fluorine, and A and B are two metals. Compared to other reduction processes, such as those involving carbon or hydrogen—where gas formation results in CO, CO_2, or H_2O—this reaction transforms the reducing metal into a solid or liquid product (Habashi, 2018). To reduce a compound, the metal must have a strong affinity, be inexpensive, possess a high boiling point and low vapor pressure, produce a slag that melts or leaches easily, avoid intermetallic compound formation, and be easy to handle. Metallothermic processes can be exothermic or endothermic. In an exothermic system, the process starts spontaneously after ignition, generating a fluid slag and a compact, homogeneous regulus of reduced metal (Habashi, 2018).

The practicality of these reactions depends on the capabilities of the reducing metal, ranked in descending order based on standard electrode potentials (e.g., Li > K > Mg > Al). However, this sequence only applies to reduction reactions in an aqueous electrolyte, not to the MRR reaction environment. In MRR reactions, the compositions and thermodynamic properties of precursors and products influence the reduction process. Thus, it is not primarily determined by metal reductants (Xing et al., 2018).

1.6.2 Exploration the Potential of Metallothermic Reduction for Sustainability

In a study by Wenzel et al. (2013), the potential application of chromium-rich ash from the thermal treatment of footwear leather waste in producing low-carbon ferrochromium alloy (Fe-Cr-LC) via aluminothermic reduction was investigated. SEM-EDS inspection of two high-conversion samples showed that the Cr level was slightly below grade A standards. While Ti levels were high, they were not harmful. However, all Fe-Cr-LC outcomes had P and S levels above permissible limits, requiring further ash pre-treatment to remove these impurities.

Furthermore, Eissa et al. (2010) examined the optimization of parameters for the aluminothermic process to create extra-low-carbon ferrochromium from low-grade chromite ore. Adjusting total input energy, flux composition and amount, and the reductant-to-ore ratio resulted in 79% chromium recovery and a 76% metallic yield in pilot plant studies. Super-low-carbon ferrochromium (0.02% C) with 61% chromium was produced using these settings on a semi-industrial scale.

In another study, Ochoa et al. (2016) examined the possibility of low-temperature ferrochrome production by reducing chromite ore with magnesium scrap as a reducing agent. The maximum Fe and Cr conversion rate was 38% at 1050°C, 3 hours, and 75% excess magnesium scrap. FeCr formed at the core of reduced particles, with layers of MgO, AlN, and $FeAl_2O_4$ developing around it. The surrounding layers blocked magnesium and aluminum from diffusing into chromite particles, resulting in incomplete reduction.

In the same context, Dávila et al. (2019) reported the effect of the presence of magnesium in molten aluminum from beverage cans on the aluminothermic reduction of Mn_2O_3 from discharged alkaline battery cathodes. This illustrates the potential for producing Al-Mn alloys while simultaneously addressing waste management issues associated with alkaline batteries. Magnesium improves aluminum's wettability on Mn_2O_3, promoting solid-liquid reactions. XRD examination revealed the presence of

MgO and $MgAl_2O_4$. Additionally, the detection of Mn_3O_4 and MnO confirms that aluminum and magnesium reduced the oxidation state of Mn_2O_3, forming intermediate manganese oxidation states during reduction.

To produce ferromanganese, Bhoi et al. (1997) investigated the aluminothermic reduction of manganese ore particles using Al powder, in combination with fluorspar and lime. Ferromanganese samples containing 70–80 wt.% Mn and 12–16 wt.% Fe were produced by conducting reduction processes during roasting at moderate temperatures of 650–950°C.

Kudyba et al. (2021) used pure aluminum and primary production aluminum dross to reduce MnO-containing slags via the aluminothermic reduction method. They formed Mn-Al alloys from synthetic CaO-MnO slag and demonstrated that charge composition affected both metal and slag composition Mn-Al-Si alloys were produced from industrial aluminum dross and ferromanganese slag with lime for minor composition adjustments. However, higher CaO levels in the slag led to increased calcium transfer to the metal. The procedure was energy-efficient and industrially flexible.

1.7 Aim of the thesis

As resource efficiency and sustainable growth become increasingly important, there is growing pressure to consider waste or by-product streams as valuable resources. Many businesses are collaborating to promote the recycling and reuse of by-products in response to the growing concept of the Circular Economy (CE) (Yao et al., 2018). The recycling strategy entails developing Industrial Symbiosis (IS) to identify new markets for waste materials beyond the manufacturing chain (Lombardi & Laybourn, 2012).

In this context, the effective transformation of steelmaking byproducts into high-value products represents both an environmental necessity and an economic opportunity. Ladle furnace (LF) slag has remained relatively unexplored in sustainability research, and its potential for valorization has not yet been fully realized. In contrast, other steelmaking slags, such as basic oxygen furnace and blast furnace slags, have received comprehensive sustainability attention. The distinctive chemical composition of ladle furnace (LF) slag—high levels of Al_2O_3 and CaO, as highlighted in earlier discussions—makes it stand out among other steelmaking slags. Given these compositional characteristics, LF slag proved to be a particularly good candidate for metallothermic reduction, making it an attractive feedstock for the production of alloys.

Ferrosilicon is an alloy of iron and silicon with an average Si concentration ranging from 15% to 90%. Ferrosilicon supplies silicon for metallothermic reductions and the deoxidation of steel and other ferrous alloys. It can be used to create further ferroalloys. Metallic silicon, corrosion-resistant high-temperature ferrous-silicon alloys, and silicon steel for electric motors and transformer cores are produced from ferrosilicon. In the process of making cast iron, ferrosilicon is mixed into the iron to speed up the graphitization process (Eric, 2014).

Calcium aluminate cement (CAC) demand has been continuously increasing (CW Group, 2023). This is primarily due to the demands of the refractory industry. Even though strength loss due to mineralogical conversions may limit its use, CAC is still preferred in specialized civil engineering applications that call for quick hardening and resistance to abrasion and sulfate attack. However, because of smaller production scales and greater raw material costs (such as bauxite), CAC usually costs four to five times as much as OPC (Scrivener et al., 1999). The carbon footprint of cement ranges from approximately 650 to 1,400 kg CO_2 per ton, depending on the alumina content (Zapata et al., 2022). Therefore, replacing some of the CAC with industrial leftovers like ladle slag (rich in alumina and calcium oxide) could help save costs and impact on the environment.

Building on this knowledge, the aim of the current thesis is valorization of LF slag through a pyrometallurgical approach by an aluminothermic reduction to transform it into a ferrosilicon alloy and a residual slag with calcium aluminate composition to be further utilized in CAC production sector. Working toward this goal, this study offers a more environmentally friendly approach for the manufacturing of silicon alloys while also advancing LF slag valorization techniques. The strategy investigated in this work supports the objectives of decarbonization, resource efficiency, and circular economy within the metallurgical industry by providing a competitive substitute for the carbon-intensive and extremely energy-demanding traditional silicon production process. Additionally, this work also aligns with the objectives of the EU H2020 SisAl Pilot project which is a unique worldwide industrial symbiosis initiative that brings together the silicon, iron, steel, and aluminum industries, by scientific and industrial method to convert low-value secondary aluminum and LF slag streams into high-value silicon products.

Thermodynamic simulations using the FactSage software, together with phase diagram analysis, enabled the selection and optimization of input materials and

conditions, for both a ferrosilicon product and a residual slag phase with compositions suitable for future industrial uses. Furthermore, to evaluate the process's scalability, efficiency, and purity, the theoretical experiment will be tested by a furnace in an experimental trial, which will be followed by spectroscopic examinations to confirm the results of metallothermic reduction in practical settings.

2 Material and Methods

2.1 Materials

For this study, four different types of steel slag—Ekominit, Reduction, Refining, and Reduction + Refining—were received for further experiments and characterization[11]. Elemental analysis was carried out with X-ray fluorescence spectroscopy (XRF), and mineralogical phases were identified and quantified by X-ray diffraction (XRD) using Co K_α radiation and the Rietveld refinement method. No internal standard was introduced during the examination; hence, it was not possible to quantitatively determine the presence and proportion of any amorphous phases.

Minor variations were observed in the chemical profiles of the Reduction, Refining, and Reduction + Refining slags. Overall, the compositional analysis of the slags provided a foundation for future research into their behavior during metallothermic reduction and their potential as feedstock materials for subsequent processing steps. Ekominit slag however, stands out from the other three samples, according to preliminary data. It displays elevated Al_2O_3 and Fe_2O_3 contents among major oxides, while SiO_2 and CaO levels tend to be lower. Minor element analysis revealed that Ekominit is enriched in Cr, Ni, Zn, and Mo, and contains higher levels of Nb, Ce, Nd, and Zr, despite having a lower fluorine content than the other slags. These compositional variations might be related to differences in steelmaking feedstocks, such as variations in ore quality or source, as well as the steel grades produced.

Two of the four slag samples were selected for in-depth analysis in order to further reduce the experimental procedure. Based on the compositional distinctions mentioned above, Ekominit slag was selected to represent the more chemically distinct category, while Reduction slag was chosen to represent the group with

[11] According to the company generating this slag, Ekominit sample is a blend of EAF and LF slag. However, due to the policy of the company, no particular information was provided by the company regarding the source of the other sample, beside the fact that they are only sourced from ladle furnace process.

generally similar, less diverse compositions. The Ekominit slag will be referred to as "Slag_E" from this point forward, and the Reduction slag will be denoted as "Slag_R" (Figure 9). The elemental compositions are presented in Table 3.

Figure 9 Visual appearance of the slag sample.

	Sio_2	TiO_2	Al_2O_3	Fe_2O_3	MnO	MgO	CaO	Na_2O	K_2O	P_2O_5	Tot	L.O.I
Slag_R (wt.%)	29.16	0.35	1.82	0.44	0.2	10.46	54.86	0.11	0.001	0.01	97.41	-
Slag_E (wt.%)	20.04	0.66	10.29	8.17	1.65	11.24	44.96	0.07	0.01	0.04	97.13	6.79

Table 3 chemical composition of chosen slag samples.

Secondary aluminum from post-consumer beverage cans served as the reducing agent in this experiment. First, the aluminum cans were cleaned and then mechanically pulverized into a uniform powder. Utilizing recycled aluminum feedstock not only reduces dependence on primary aluminum ores but also helps close the material loop, aligning the process with sustainability and circular economy principles. This approach enhances resource efficiency in metal manufacturing by utilizing an existing waste stream—discarded beverage cans—and transforming it into a valuable metallurgical input (Figure 10). The chemical composition of the secondary aluminum is displayed in Table 4.

Al	Al_2O_3	Mg	Mn
85.2%	10%	4.5%	0.3%

Table 4 chemical composition of secondary aluminum (wt.%).

Figure 10 Secondary aluminum reagent used.

Iron and steel scrap, produced as a by-product of final shaping operations in a steel mill, served as the metal charge. Trimming steel products produces thin, helical, ribbon-like strips, commonly referred to as scrap. No post-collection cleaning, sorting, or size reduction was performed; the materials were used directly from the manufacturing line. Although its composition is expected to be generally homogeneous due to its controlled origin, the lack of pretreatment may result in residues of surface oxidation or other production-related impurities (Figure 11). The chemical composition of iron scrap is presented in Table 5.

Fe	Fe_2O_3
90%	10%

Table 5 Chemical composition of iron scrap (wt.%).

The silica addition in this reaction was done with silica sand, the composition of which is displayed in Table 6.

Compound	**Wt.%**	**Est. Error**
SiO_2	85.22	0.18
Al_2O_3	7.91	0.13
K_2O	2.17	0.07
Na_2O	1.34	0.06
Fe_2O_3	1.26	0.06

Table 6 Chemical composition of silica sand (wt.%)

Figure 11 Iron scrap used (left) and silica source (right).

2.2 Methods

2.2.1 Thermodynamic Basis: The Ellingham Diagram

A fundamental step in designing and evaluating metallothermic reduction processes is to understand the relative stability of various metal oxides and the feasibility of their reduction. The Ellingham diagram illustrates the Gibbs free energy changes (ΔG) related to oxide formation reactions as a function of temperature, helping researchers determine which oxides can be reduced by a given reductant under specific conditions. An Ellingham diagram is a temperature-versus-Gibbs-free-energy graph for oxidation reactions, often standardized to the reaction of one mole of O_2. Conventionally, ΔG=0 is set at the top of the diagram; therefore, the vertical axis (ΔG) often shows values below zero, with rising negative values extending below. This is decided as most metal oxides formation from their constituent metals and oxygen is energetically favorable (negative ΔG). Each metal-oxide pair is represented by a straight or slightly curved line, where the slope reflects entropy changes, and the y-intercept corresponds to the enthalpy of formation. Any phase changes, like melting or vaporization, can alter the line's slope, as temperature affects both ΔH and ΔS.

Metals positioned lower on the Ellingham diagram (i.e., with more negative ΔG values) tend to form more stable oxides at a given temperature. A metal can theoretically reduce the oxide of another metal if the latter's line is positioned above its own, since the reducing metal's oxide is thermodynamically more stable. Aluminum, for instance, can act as an effective reducing agent for a variety of other metal oxides since it creates a highly stable oxide form and is located around the lowest points on the

diagram. However, under normal circumstances, aluminum cannot reduce oxides that are below its line as they are more stable than aluminum oxide (Figure 12).

The Ellingham diagram also provides insight into how gas species interact. Most metal-oxide lines, for example, have an upward slope since the reaction decreases entropy by transforming a gas (O_2) and a condensed phase into a condensed oxide. However, lines associated with carbon oxidation reactions are an exception. The carbon-to-CO_2 and carbon-to-CO lines appear as nearly horizontal and downward-sloping respectively, due to changes in entropy associated with gas formation. This possible intersection of carbon, particularly the descending one, with other lines at various temperatures explains why carbon is frequently employed as a reductant in many metallurgical processes (Transactions and Communications, 1944).

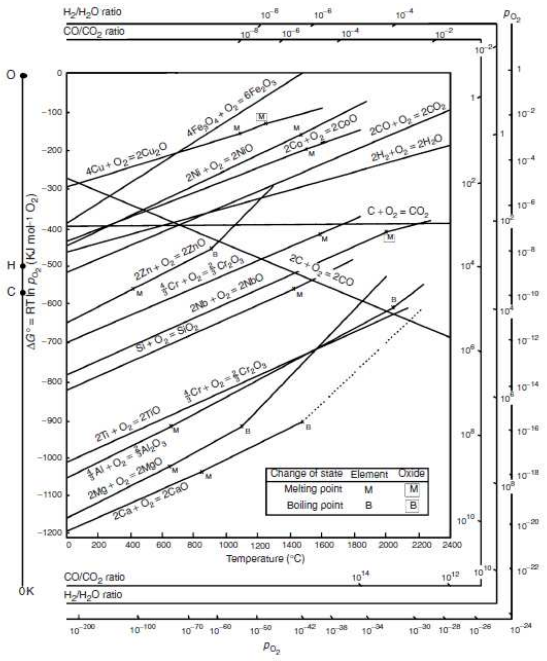

Figure 12 Ellingham diagram left (Ali & Akhtar, 2015), right (Ellingham Diagram - Thermodynamics Principle of Metallurgy, 2022).

2.2.2 Application to Aluminothermic Reduction of Steelmaking Slag

The Ellingham diagram was used in this work as a theoretical foundation for selecting the reductant to produce ferrosilicon alloys from steelmaking slag. Aluminum's low position on the Ellingham diagram clearly indicates its strong thermodynamic potential to reduce most of the metal oxides found in the studied slags like silica, manganese, iron and chromium oxides to their respective metallic forms, resulting in an alloy enriched with Fe, Si, Mn, as well as Cr. The reduced alloy phase, which is the final

product of the aluminothermic reduction process and primarily consists of iron (Fe) and silicon (Si), will be referred to as ferrosilicon from this point forward.

However, not all oxides present in the slag are positioned above aluminum on the Ellingham diagram. Under the given conditions, it is impossible to reduce oxides of Calcium and Magnesium, as their formation energy is even more negative than that of Al_2O_3. As a result, these species stay oxidized in the residual slag phase generated during this reduction reaction. In addition to these oxides, the aluminum after being consumed as reducing agent, undergoes transformation into Al_2O_3 (alumina), which appears in the residual slag as well.

At the end of the redox reaction, the system splits into a slag phase that now comprises alumina and other oxides that are too stable to be reduced, as well as a ferrosilicon rich in iron and silicon (and other metals reduced by aluminum).

A ternary phase diagram approach has been used to complete the knowledge obtained from the Ellingham diagram, allowing the selection and optimization of input materials. Ternary phase diagram is a graphical representation of a system made of three components, showing equilibrium phases or their composition regions, with respect to pressure and temperature. Each vertex of the diagram refers to a pure component, while any point within the triangle represents a mixture of the three components, specifically CaO, MgO, and Al_2O_3 in this case, with the coordination of the point reflecting their relative molar fraction in the system (Figure 13).

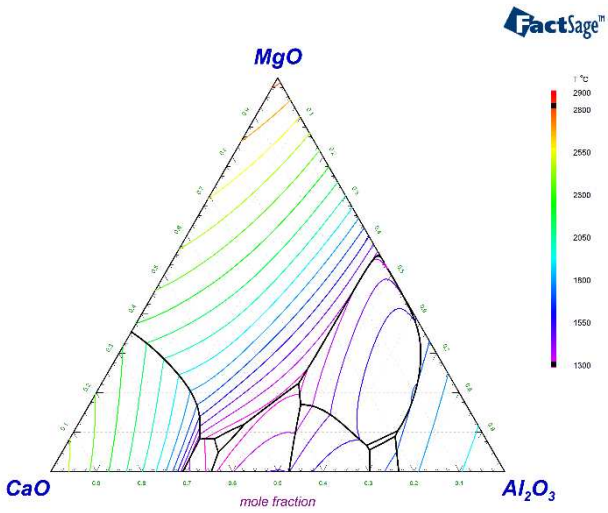

Figure 13 Ternary Phase diagram of CaO, Al_2O_3, and MgO.

The motivation of ternary phase diagram adoption was driven by broadening the overall metallurgical process's sustainability and circularity scope, by implementing a

thermodynamic approach that goes beyond only metal extraction and includes strategic management of slag composition. This strategy enhances circular economy principles and resource efficiency by producing by-products that are more suitable for subsequent recovery or valorization processes. It is possible to shift residual slag's composition toward a target phase region with desirable qualities for downstream uses by carefully modifying the input elements.

As mentioned earlier, the ferrosilicon alloy is formed by reducing the oxides (e.g., iron oxides, silica) to metallic forms in the aluminothermic reduction process. The relative stability of CaO and MgO, however, results in little to no reduction through this process, providing a pathway on the phase diagram to shift the composition of the slag. The main variable that can move the composition of the residual slag to the desired region on the phase diagram, based on the given situation, is Al_2O_3 (alumina) content (Figure 14).

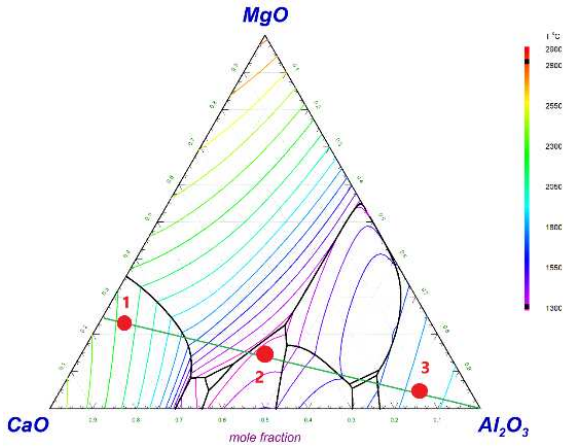

Figure 14 Alumina addition allows to shift the slag composition from point 1 to 3, or any points in between.

Plotting the slag's original composition[12] on the CaO-MgO-Al_2O_3 ternary diagram allows one to see this pathway and to observe how the system's composition changes with applying adjustments to the Al_2O_3 share in the system. The objective is to shift the initial composition to the calcium aluminate region in this case, which is known to be advantageous for further downstream applications (Figure 15). Aluminum is the main source of alumina (Al_2O_3) by converting SiO_2 (and other oxides) to their metallic state, generating alumina as a consequence. However, depending on where the initial

12 Although the slag is made up of various compounds, however, a ternary phase diagram made of CaO-MgO-Al_2O_3 was chosen to analyze because these compounds represent the major constituent of the slag. Additionally, the residual slag would have the same composition based on the Ellingham's diagram.

composition of slag falls within the phase diagram, three main scenarios are expected to happen when increasing the share of alumina inside the system.

First, after adding enough aluminum to fully reduce all of the oxides in the system, the alumina content allows the final slag composition to stay within the targeted phase region. In this case no further actions are required. Second, the ultimate slag composition (after reducing all of the oxides) falls beyond the desired region, which calls for a lower alumina share in the system; this is simply achieved by introducing less aluminum in the system. Some unreduced oxides presence in the residual slag phase would be inevitable in this situation due to lack of adequate reducing agent. Lastly, the alumina fraction is not sufficient to meet the sought composition area, requiring an excess amount of alumina to push the left-behind composition towards its final destination.

In the context of this work, the last scenario was witnessed across both Slag_E and Slag_R. Simultaneous silica and aluminum addition were taken into consideration to fulfill the excess alumina requirement of the system[13]. The additional silica and aluminum undergo a reaction, solving the alumina Al_2O_3 deficiency as well as providing more metallic silicon for the ferrosilicon alloy upon its formation. By means of this co-adjustment, the slag's composition can be redirected into the calcium aluminate-rich region of the ternary diagram.

2.2.3 Optimizing Residual Slag Composition of Slag_R

A high-quality ferrosilicon product and reusable slag phase require accurate residual slag composition control. This section focuses on the CaO-MgO-Al_2O_3 ternary system to discuss the residual slag, as other oxides are either converted to metallic forms or present in negligible concentrations. The initial composition of the Slag_R is characterized by a majority of CaO, followed by MgO and just a small fraction of Al_2O_3. Plotting this initial composition on the CaO-MgO-Al_2O_3 ternary diagram creates a baseline for tracking future changes (see point 1 in Figure 15).

When aluminum is added, reducible oxides including SiO_2, Fe_2O_3, MnO, and Cr_2O_3 reduce to respective metals, resulting in Al_2O_3. A more detailed demonstration of the calculation is presented in Table 8. By taking this approach, it is expected that the

[13] This addition was done in a way that all of the added aluminum reduces silica, that there is nothing added to the system beside metallic silicon and alumina. According to the stoichiometric of the redox reaction of silica and aluminum, every gram of aluminum is capable of reducing 1.67 grams of silica.

composition of slag moves toward the Al_2O_3 vertex of the ternary diagram as the fraction of alumina grows on a straight line considering the constant ratio of CaO and MgO. Plotting this new point on the phase diagram (see point 2 in Figure 15), the lacking alumina fraction in order to accomplish calcium aluminate region is visible. Silica and aluminum can be added simultaneously to push this threshold to meet calcium aluminate area (see point 3 in Figure 15). According to calculations[14], an extra 22 grams of aluminum are needed to reach the destination.

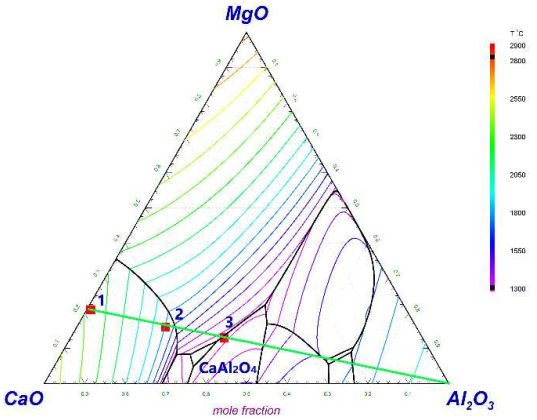

Figure 15 schematic representation of aluminum addition. Point 1 represents the initial composition of slag sample(before starting the process), point 2 represents the composition after reducing all of the oxide and point 3 stands for the final desired region.

Phase Description	Al_2O_3	CaO	MgO
Initial Slag Composition	0.01	0.78	0.21
After Reduction of Oxides	0.22	0.62	0.16
Calcium Aluminate Phase	0.38	0.49	0.13

Table 7 Calculating the coordination to plot them on Phase diagram.

oxides to be reduce	Mass of reducing agent	Mass of alumina generated
silica	17.47	32.99
titanium dioxide	0.1577	0.2976
iron (III) oxide	0.149	0.2804
manganese oxide	0.051	0.096
Chromium(III) oxide	0.1242	0.2345
Total	17.9519	33.8985

Table 8 Stoichiometric calculation for reduction of respective phases in aluminothermic reduction optimization.

[14] This calculation was mainly obtained from the phase diagram and based a series of trials and errors in the thermodynamic simulation of the system with constantly monitoring the composition of slag and optimizing it furthermore to reach the optimal results.

2.2.4 Optimizing Residual Slag Composition of Slag_E

The starting point for Slag_E is slightly different from that of the previously studied sample. Its initial chemistry shows a relatively lower quantity of CaO and a larger fraction of Al_2O_3. The baseline location of the initial slag is already closer to the calcium aluminate region than the other slag when presented on the CaO-MgO-Al_2O_3 ternary diagram (Figure 16). This situation requires less extra alumina addition to reach the required phase field (17 grams) compared to the previous sample.

oxides to be reduce	Mass of reducing agent	Mass of alumina generated
silica	11.99	22.67
titanium dioxide	0.297	0.562
iron (III) oxide	2.76	5.22
manganese oxide	0.42	0.79
Chromium(III) oxide	1.49	0.2.17
Total	16.9	31.41

Table 9 Stoichiometric calculation for reduction of respective phases in aluminothermic reduction optimization.

Phase Description	Al_2O_3	CaO	MgO
Before Addition of Aluminum	0.09	0.68	0.23
After Reduction of Oxides	0.27	0.54	0.19
Calcium Aluminate Phase	0.4	0.45	0.15

Table 10 Calculating the coordination to plot them on Phase diagram.

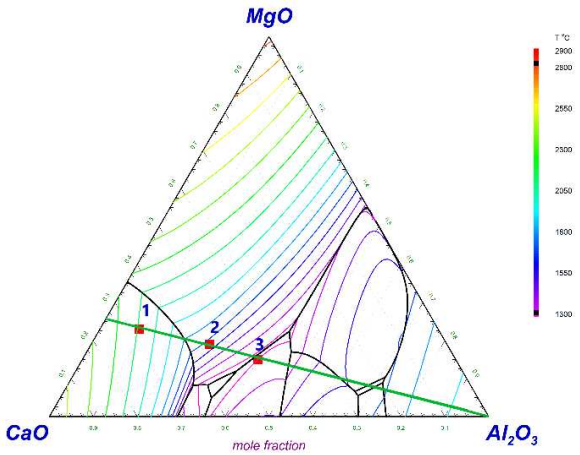

Figure 16 schematic representation of aluminum addition. Point 1 represents the initial composition of slag sample, point 2 represses the composition after reducing all of the oxide, and point 3 stands for the final desired point.

2.2.5 Thermodynamic simulation and ferrosilicon composition adjustment

The aluminothermic reduction process was carefully monitored, and the ferrosilicon composition was adjusted with the help of thermodynamic simulation performed by FactSage software. The Equilib module in FactSage software was utilized to model the system's thermodynamic behavior. The appropriate phases, temperature ranges, and phase modes were selected to record the formation and transformation of oxide and metallic species during the reduction.

Two separate sets of inputs were introduced to start the simulations. To accurately represent the molten condition of the process environment, the slag sample compositional compounds were first added at 1500°C. Following that, the additions of iron, silica, and aluminum—which are necessary to propel the reduction reactions and adjust the ferrosilicon composition—were added at room temperature. These varying temperature inputs enable the software to calculate the energy and mass exchanges that occur as the reducing agents and alloying ingredients integrate into the molten slag.

In order to obtain the necessary ferrosilicon composition, iron additions were required. Multiple tests were conducted out to determine the optimal quantity of iron required to achieve desired alloy grades, such as FeSi25. By evaluating the amount of silicon that originates from two sources—silicon reduced from the slag's inherent silica content and silicon formed during the extra aluminum addition—an optimal iron-to-silicon ratio was found. By following this technique, the ferrosilicon alloy grade can be consistently monitored.

The FactSage equilibrium simulations provide complete details about the process's developing chemistry. These computations could be used to track the changes in composition at each temperature interval, trace the emergence and disappearance of particular phases, and identify the exact distribution of components between the metal and slag phases. The final equilibrium composition of the ferrosilicon alloy and the remaining slag, along with concentration profiles for each phase over the temperature ranges under study, are included in the results as well. By ensuring that the thermodynamic conditions are in line with the goals of creating high-quality ferrosilicon while maintaining a residual slag composition appropriate for later reuse or recycling, this level of information allows making accurate choices regarding the process parameters (Figure 18).

Thermodynamic simulation was carried out on the slag samples using a set of inputs to make a ferrosilicon with 25% silicon complying with ISO 5445-1980 (Figure 17), while ensuring that the final slag composition of the process falls within the calcium aluminate region.

Designation	Chemical composition, %									
	Si		Al		P	S	C	Mn[1)]	Cr[1)]	Ti[1)]
	over	up to and including	over	up to and including	max.	max.	max.	max.	max.	max.
FeSi10	8,0	13,0	–	0,2	0,15	0,06	2,0	3,0	0,8	0,30
FeSi15	14,0	20,0	–	1,0	0,15	0,06	1,5	1,5	0,8	0,30
FeSi25	20,0	30,0	–	1,5	0,15	0,06	1,0	1,0	0,8	0,30
FeSi45	41,0	47,0	–	2,0	0,05	0,05	0,20	1,0	0,5	0,30
FeSi50	47,0	51,0	–	1,5	0,05	0,05	0,20	0,8	0,5	0,30
FeSi65	63,0	68,0	–	2,0	0,05	0,04	0,20	0,4	0,4	0,30

Figure 17 ISO 5445-190 product specification.

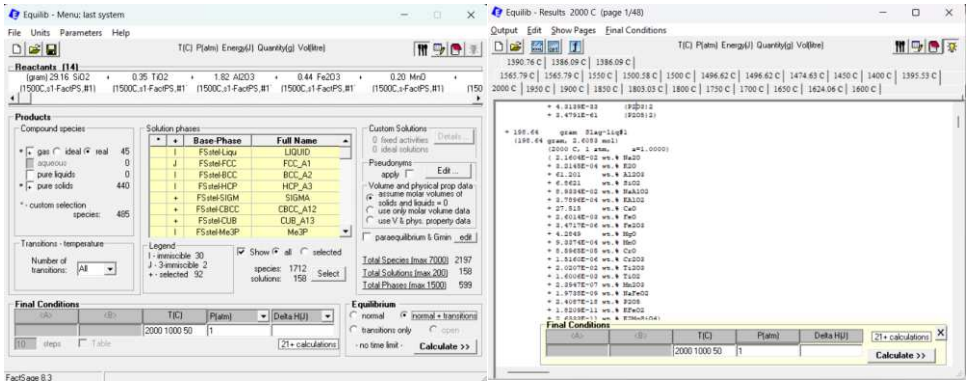

Figure 18 Snapshot of the Equilib window interface showing the inputs, phases and other settings (left); Snapshot of the results, compositional breakdown of every phase at different temperatures are provided in the result window (right).

2.2.6 **Experimental Validation of Thermodynamic Simulations**

The experiment started with weighing each sample with a HZ30002B electric balance (maximum capacity of 3000 g, e = 0.1, d = 0.01, accuracy Class III). For each sample, a ceramic crucible with 100ml of volume (Figure 19) was chosen so that the experiment would be carried out with lower energy requirement as a result of a facilitated melting owing to minimal charge. For the aluminothermic reduction of Slag_R, 20 grams of slag sample, 8.8 grams of secondary aluminum, 15.4 grams of secondary iron, and 9 grams of silica sand were measured. In the second set, 25 grams of Slag_R, 9 grams of secondary aluminum, 16.75 grams of secondary iron, and 9.25 grams of silica sand were put in to the crucible[15].

[15] The difference between the amount of inputs charged to the furnace and values given to FactSage software to carry out the simulations in the simulation is due to using secondary materials that represented some impurity. Compared to the simulation, where the software considers the inputs in 100% pure form, the furnace must be charged with more quantity of the materials to make up the deficiency. The calculations are based on the composition of the secondary material reported in Table 4 to Table 6.

Since the secondary iron was greasy, it was put in the furnace for a short time (about five minutes) until flames started to coming out from the hole in on the lid, signaling that the oil had been burned off. To avoid any potential localized overheating or splattering, all ingredients were mixed properly to ensure an even distribution (Figure 19). The two ceramic crucibles were set in the middle of a furnace that was powered by two gas capsules of GPL (Figure 20 and Figure 21). To avoid blowing out or prematurely igniting small particles, particularly aluminum, the gas pressure was initially maintained at 0.1 MPa for five minutes. Following that short interval, the pressure was increased to 0.2 MPa. Every 10 minutes, the pressure was gradually reduced, the furnace lid was lifted, and the process was examined. The furnace ran for thirty minutes before being turned off. Safety precautions, such as wearing protective gloves and wrapping a piece of cloth around the gas line to reduce the possibility of leaks or explosions, were closely followed throughout the procedure.

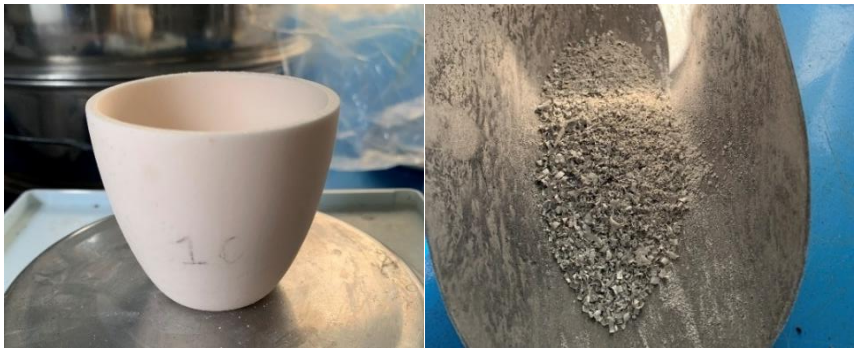

Figure 19 Crucibles used for this experiment (left); the mixed charge (right).

Figure 20 visual appearance of the furnace (left), internal part of the furnace (right).

Figure 21 sample placement in the furnace (left), after the heating (right).

The samples were quickly cooled with water after coming out of the furnace. Following that, the crucibles were carefully hammered to loosen the sample, which proved to be difficult because of strong sample adherence to the crucible walls (Figure 22). Visual inspection was used to separate the metallic-looking portions of the sample from the slag after hammering (Figure 23). The sample was then ready for grinding using a typical steel cylinder combined with agate mortar. The bigger particle size of the metallic spheres made them simpler to separate from the slag after further hammering (Figure 23). During this phase, the materials were in semi-powdered form, but the metallic component remained mixed with the slag by a bigger and shinier particle appearance. A manual magnetic separation technique was used in order to separate them.

Figure 22 A close look at the crucible after cooling down (left); visible adhesion of the heated sample to the crucibles walls (right).

Figure 23 A clear distinction between the metallic phase and the residual slag : areas indicated by the number 1 shows the metallic phase while the residual slag is visible (left); metallic spheres separated from the sample (right).

The samples were sorted using three different mesh sizes of sieves to ensure optimal separation. The separation of the metallic particles was done by using a 1 mm mesh. Mesh sizes of 500 and 180 µm were utilized to filter the metal and slag mixture by manual rotation of the discs (Figure 24). the final powder was successfully separated through passing a sieve size of 180 µm at the bottom of the filter. To guarantee the proper segregation of the slag and metallic components, this separation procedure of hammering, magnetic separation and sieving was carried out several times. Some shining substance particles showed that certain metallic components were still embedded in the slag powder despite these repeated attempts, suggesting slight interferences in the finished slag mixture. This residual slag was prepared for XRD analysis through a series of sample preparation steps, while the metallic spheres were further analyzed using SEM. Additionally, to better evaluate the results from XRD, the slag was also sent for XRF analysis to serve as complementary data for XRD (Figure 24 and Figure 25).

Figure 24 Continuous hammering, griding and sieving enabled the bigger metallic material separation (left) from the residual slag (right).

Figure 25 The pulverized slag after sieving for a smooth surface (tiny shiny particles of metallic phase is visible) (left); the slag (darker particles) + metallic phase (shiny particles) with the dimension of 180 µm (right).

Figure 26 Samples prepared for XRD analysis.

2.2.7 Spectroscopy Analysis; An Overview

X-ray fluorescence (XRF) is one of the most powerful analytical methods for identifying the chemical composition of materials. Examples of areas in which XRF its major application are environmental monitoring, material science, and metallurgical sectors. The high-energy X-rays coming from a source, usually an X-ray tube, hits inner-shell electrons and kick one out, leaving a hole in that particular orbital. These are subsequently filled by higher-energy electrons, resulting in emission of a secondary X-rays which is unique to the elements under analysis. The precision in XRF comes from an atom-based interaction, being able to distinguish the specific peaks coming from atomic transitions like Kα and Kβ separately. Qualitative analysis uses X-ray energy to identify elements, whereas quantitative analysis uses intensity to determine element concentration. This information can be seen as peaks in a spectrum, with the position of the peaks representing the energy of the emitted X-rays, which is unique for each element, and the height of the peaks reflecting their abundance in the sample (Brouwer, 2003). The sample preparation of residual slag for XRF analysis has been done by technicians of Geoscience Department of University of Padova.

A common non-destructive analytical method for studying a material's crystalline structure is X-ray diffraction (XRD). A standard XRD system involves an X-ray source, a sample stage, a goniometer for precise angle measurements, and a detector to capture diffracted beams. The angles and intensities of the diffracted beams from atomic planes in a crystal lattice is defined by Bragg's Law ($n\lambda=2d\sin\theta$). Each material's diffraction patterns are unique and form peaks whose locations reflect lattice spacings, with their intensities showing the relative abundance of crystallographic orientations.

The size of crystallites determines the width of this peak. While a narrow peak refers to large grains, finer crystallites show wider peaks, as seen in nanostructured materials. Therefore, variations in the width of peaks can pinpoint the lattice strain or defects, probably because of mechanical stresses within the crystal lattice. Analysis of amorphous phases is possible where sharp peaks are replaced by diffused one via evaluating peak characteristics , shape, and position. Features such as these make XRD a crucial tool in not only the identification of phases but also in the assessment of structural features affecting material properties (Harrington & Santiso, 2021). Following the grinding process, after washing the samples with ethanol and drying

them with infra-red lamp, each powdered sample was evenly distributed onto a back-loaded sample holder and pressed into a pellet for XRD analysis (Figure 26).
According to Morgan and Chau (2021), scanning electron microscopy (SEM) employs a precisely focused electron beam to scan a material's surface, creating secondary or backscattered electrons that show its shape and structure at high magnification. In parallel, energy-dispersive X-ray spectroscopy (EDS) analyzes distinctive X-rays generated when the electron beam dislodges electrons from sample atoms, identifying the elements. SEM photography and EDS analysis allow researchers to map a material's chemical composition and surface characteristics in one instrument. Sample preparation for SEM was handled by technicians from the Engineering Department of the University of Padova, ensuring consistent mounting and coating procedures according to standard operating protocols.

Figure 27 Polishing device, used to cut and shape the sample to desired size for an effective resin embedding (left), final sample embedded in resin (right).

3 Results

3.1 Phase Analysis of Slag_R

This section is dedicated to the phase analysis of the thermodynamic simulation carried out on Slag_R sample. The inputs are shown in Table 11.

Constituents	Amount (g)	Temperature (°C)	Stream
SiO_2	29.16	1500	1
TiO_2	0.35	1500	1
Al_2O_3	1.82	1500	1
Fe_2O_3	0.44	1500	1
MnO	0.2	1500	1
MgO	10.46	1500	1
CaO	54.86	1500	1
Na2O	0.11	1500	1
K_2O	0.001	1500	1
P_2O_5	0.01	1500	1
Cr_2O_3	0.2392	1500	1
Al	40.95	25	2
Fe	91.2	25	2
SiO_2	38.41	25	2

Table 11 inputs used for thermodynamic simulation.

Starting from temperature 2000°C, the system is mainly composed of three phases: a residual slag (referred to simply as "slag"), along with two molten metallic phases, identified as "Liquid#1" and “Fe-liq”[16]. From this temperature, all of the introduced phases start interacting, but the Fe-liq transformation into Liquid#1 bears the most importance. During this process, the metallic aluminum in Fe-liq reduces silica content of the slag, leading to formation of additional alumina within the slag phase, and simultaneous metallic silicon accumulation in Liquid#1. This exchange lasts until the temperature 1841.21°C where Fe-liq reaches zero in concentration (Figure 28).

Between 1841.21°C and approximately 1500°C, the same reduction mechanism was persistent between Liquid#1 and slag phase, with aluminum content of Liquid#1 reducing the silica from the slag.

According to this pattern, the remaining metallic aluminum in molten phases are acting as a reducing agent, reducing the silica in the slag and transferring it to Liquid#1 as metallic silicon. Despite confirming the reduction process, it is essential to note that these compositional changes resulting from the reduction process are small when compared to the interaction of the Fe-liq and Liquid#1 phases (as seen in Figure 3), therefore, the contributions to the system are minimal (Figure 29).

[16] The slag phase can be broadly described as a quaternary system containing Al_2O_3, CaO, SiO_2, and MgO. In contrast, the molten metallic phase encompasses multiple metallic elements, primarily iron, silicon, aluminum, and chromium. However, because these phases undergo continuous chemical interactions across the investigated temperature range, the exact proportions of each element or compound in any given phase cannot quantitatively be reported quantitatively at a single temperature.

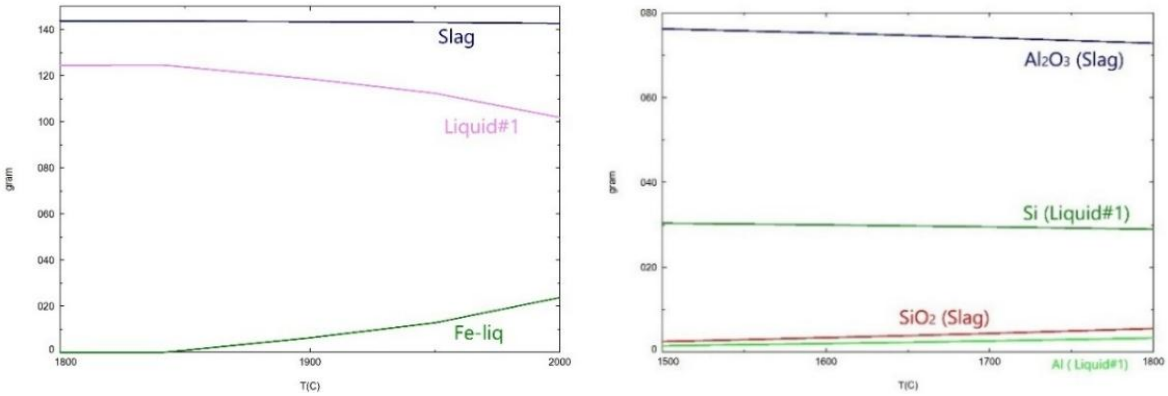

Figure 28 A general view of system interaction between phases Fe-liq, Liquid#1 and slag (top); a more detailed analysis of the same phases across a wider temperature range (bottom).

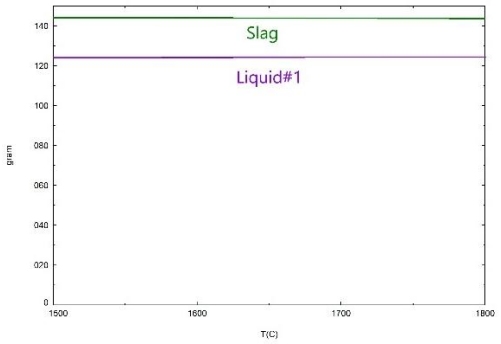

PHASE: LIQUID#1	gram		WEIGTH %		ACTIVITY	
Al	1.4103E+00	- 2.2014E+00	1.1373E+00	- 1.7628E+00	7.4001E-03	- 1.7047E-02
Cr	1.6366E-01	+ 4.1800E-05	1.3197E-01	+ 5.9810E-04	5.5696E-04	+ 6.5440E-05
Fe	9.1508E+01	+ 8.7000E-04	7.3792E+01	+ 3.1635E-01	1.5812E-01	- 6.5678E-02
Mn	1.5485E-01	+ 4.0060E-04	1.2487E-01	+ 8.5580E-04	3.6743E-04	- 1.3854E-04
Si	3.0489E+01	+ 1.7506E+00	2.4586E+01	+ 1.5108E+00	2.7956E-02	- 1.9305E-02
Ti	2.0025E-01	+ 2.4496E-02	1.6148E-01	+ 2.0360E-02	2.5451E-06	- 7.3426E-06
TOTAL :	1.2401E+02	- 5.3270E-01	1.0000E+00	-	1.0000E+00	+ 0.0000E+00
PHASE: LIQUID#2	gram		WEIGTH %		ACTIVITY	
Al	0.0000E+00	+ 0.0000E+00	1.1373E+00	+ 1.0893E+00	7.4001E-03	- 1.7047E-02
Cr	0.0000E+00	+ 0.0000E+00	1.3197E-01	+ 1.3164E-01	5.5696E-04	+ 6.5440E-05
Fe	0.0000E+00	+ 0.0000E+00	7.3792E+01	- 2.3714E+01	1.5812E-01	- 6.5678E-02
Mn	0.0000E+00	+ 0.0000E+00	1.2487E-01	+ 1.2459E-01	3.6743E-04	- 1.3854E-04
Si	0.0000E+00	+ 0.0000E+00	2.4586E+01	+ 3.0631E+00	2.7956E-02	- 1.9305E-02
Ti	0.0000E+00	+ 0.0000E+00	1.6148E-01	+ 1.6094E-01	2.5451E-06	- 7.3426E-06
TOTAL :	0.0000E+00	+ 0.0000E+00	1.0000E+00	-	1.0000E+00	+ 0.0000E+00
PHASE: Slag-liq#1	gram		WEIGTH %		ACTIVITY	
Al2O3	7.6406E+01	+ 4.1426E+00	5.2985E+01	+ 2.6870E+00	1.1387E-02	- 2.3534E-02
SiO2	2.3432E+00	- 3.7451E+00	1.6249E+00	- 2.6128E+00	1.8996E-04	- 3.0536E-04
NaAlO2	1.9759E-01	+ 2.7312E-02	1.3702E-01	+ 1.8502E-02	4.2666E-04	- 9.9075E-06
CaO	5.4787E+01	+ 9.8780E-02	3.7993E+01	- 7.2130E-02	3.2421E-02	- 3.5333E-02
MgO	1.0417E+01	+ 5.8400E-02	7.2240E+00	+ 1.3857E-02	7.2074E-02	- 1.2503E-03
TOTAL :	1.4420E+02	+ 5.3270E-01	1.0000E+00	-	1.0000E+00	+ 0.0000E+00

Figure 29 Slag and Liquid interaction (left); XML window featuring the mass balance of compound exchanges between slag and Liquid#1 from 1841.21 to 1500°C (right).

Between 1500°C and 1300°C, the slag gradually transforms into several distinct phases based on its composition. Ti-Spinel#1 is the first one, emerging at around 1478.06°C, as shown in Figure 30. A calcium aluminate ($CaAl_2O_4$) phase occurs next at around 1374.5°C, and at approximately 1334.07°C, calcium magnesium aluminate ($Ca_3MgAl_4O_{10}$) is eventually formed. By inspecting the concentration profiles in Figure 30, it is apparent that there is a drop in the line representing the mass of the slag phase right in the moment where a new phase starts to form from the bottom of the graph. Thus, it can be concluded that the slag phase is the source of the emergence of these phases. These findings are confirmed by the data obtained from the XML window and the respective mass balance calculations. The energy balance of the system shows that the exothermicity of the reaction is 334.42J/g, equivalent to 92.9kWh/ton.

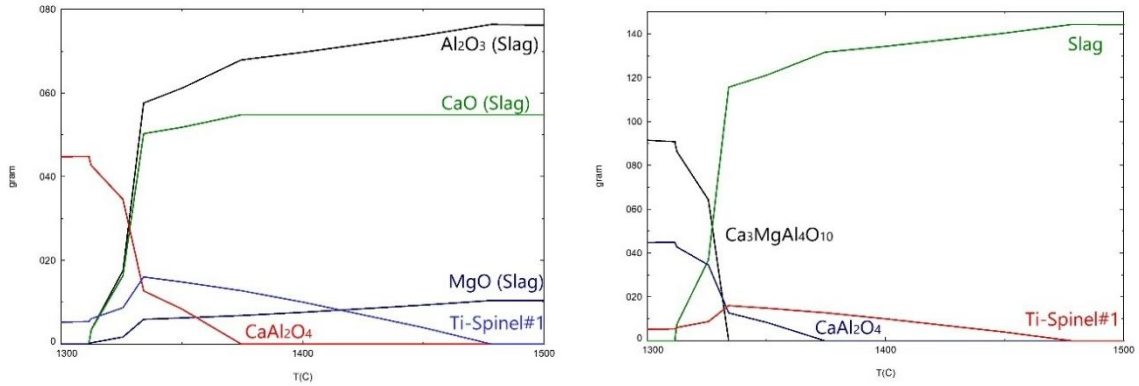

Figure 30 Transformation of slag into various phases (left); A more detailed view of compounds consumed for each phase formation (right).

A more detailed view on these changes is provided in Figure. Ti-Spinel#1 is mainly made up of magnesium and aluminum-bearing compounds, resulting in a decrease in Al_2O_3 and MgO content within the slag upon its formation. Similarly, the fact that CaO and Al_2O_3 levels drop at the same time as $CaAl_2O_4$ forms indicates that these elements are being utilized to form this phase.

As shown in Figure 30, the precipitation of $Ca_3MgAl_4O_{10}$ has the most significant impact on the mass of the slag among the emerging phases, causing a sharp drop in the slag concentration line. Figure 31 shows this process even more clearly: the system takes Al_2O_3, CaO, and MgO from the slag plus Ti-Spinel#1 to make $Ca_3MgAl_4O_{10}$ precipitate[17]. The slag stops interacting with the system after it is fully consumed (at about 1308.3°C) by these formed phases. Relative stability of the formed phase until end of the simulation was observed.

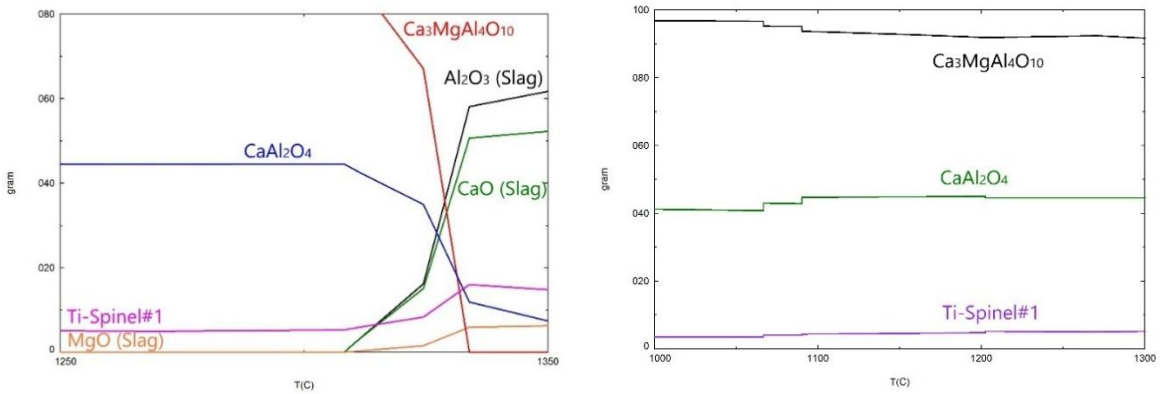

Figure 31 compound exchange to form calcium magnesium aluminate (top); concentration profile of the formed phases until the end of the simulation (bottom).

[17] However, not all of these compounds precipitate as calcium magnesium aluminate phase. A portion of the Al_2O_3 along with CaO are transferring to $CaAl_2O_4$ phase, leading to a sharp increase in the calcium aluminate mass in the same temperature.

Focusing on the metallic part of the system, Liquid#1 shows relative stability between 1500°C to 1300°C. But as Figure 9 demonstrates, it transforms into the Me_1Si_1 mostly of made of FeSi) phase at about 1306.07°C, followed by precipitating as solid Fe_2Si at 1180.43°C. the newly formed Fe_2Si solid phase gains considerable mass in small temperature interval, but it gets dissolved completely in the following emerging phases: M_5Si_3 (made mostly of FeSi) forming at 1142.1°C and BCC2#1 appearing at 1123.92°C[18] (Figure 32).

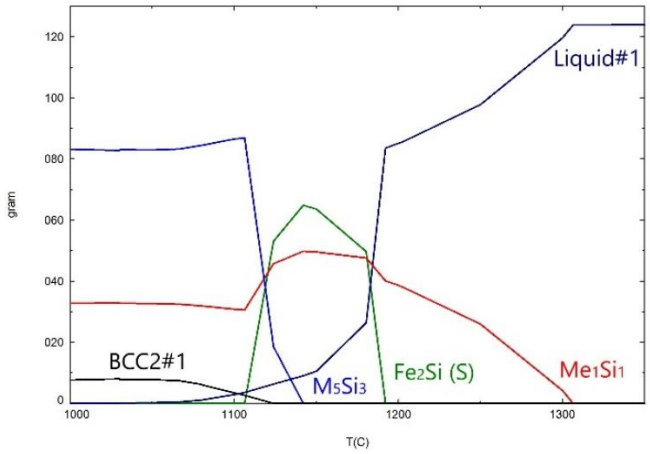

Figure 32 Emerged phase during Liquid#1 cooldown.

The thermodynamic simulation provides the mass, compositional breakdown and other information of each phase at various temperatures. By analyzing the composition of the slag phase and plotting them on ternary (between MgO, CaO, and Al_2O_3) and quaternary (between $Ca_{(x)}Mg_{(y)}O$[19], Al_2O_3 and SiO_2) phase diagram, it is clear that the composition of slag in the slag forming temperatures falls within the desired calcium aluminate region (Figure 33). The composition of slag can be found in Table 12.

For the product of this process, the phase Liquid#1 was taken into consideration. As it can be seen by Figure, a ferrosilicon with 25% silicon and 75% iron was obtained within the slag-forming temperature ranges (Table 13).

[18] Me_1Si_1 is a phase which its compounds are made of metal and silicon in 1:1 ratio, such as FeSi (highest portion), CrSi and MnSi (with lower share). M_5Si_3 is can be is similar to Me1Si1 but it shows a 5:3 metal-to-silicon. BCC2#1 is made of $SiFeva_6$, $FeFeVa_6$ and $AlFeVa_6$ in lower share.

[19] CaO and MgO were considered as one compounds where "x" and "y" represents the molar fraction of CaO and MgO respectively inside a binary system of Cao and MgO.

SiO_2	1.62
TiO_2	-
Al_2O_3	52.98
Fe_2O_3	-
MnO	-
MgO	7.22
CaO	37.99
Na_2O	0.02
K_2O	-
P_2O_5	-

Table 12 Residual slag composition within slag-forming temperatures.

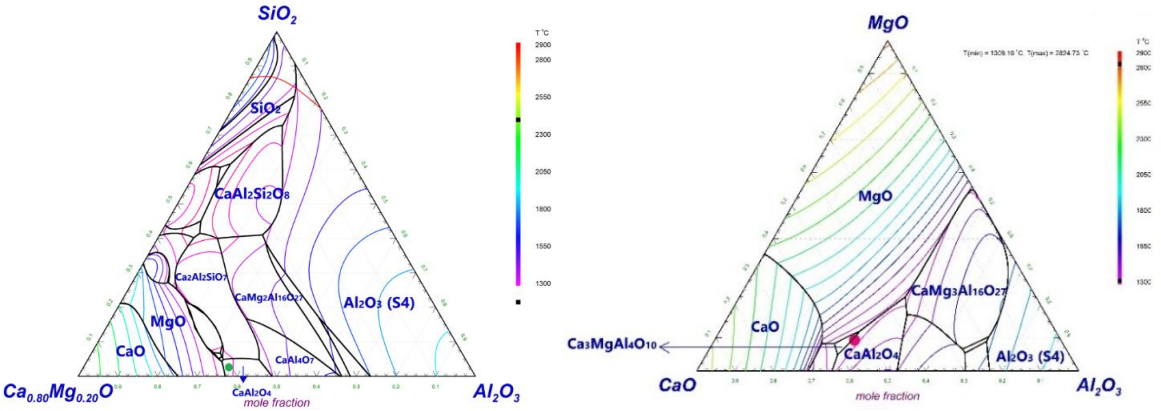

Figure 33 Ternary phase diagram and the marked point corresponding to slag composition (top); quaternary phase diagram of the same slag with marked point representing the composition (bottom).

Elements	Wt.%
Al	0.86
Cr	0.13
Fe	73.83
Mn	0.12
Si	24.82

Table 13 Metallic liquid (Liquid#1) composition.

3.2 Phase Analysis of Slag_E

Liquid#1, Fe-liq, and slag are the three distinct phases that coexist in the thermodynamic simulation (see Table 14) of this sample from 2000°C. Although there are interactions between all three phases, the most significant exchange occurs with the transfer of Fe-liq into Liquid#1. Furthermore, a small quantity of metallic aluminum in Fe-liq reduces the silica levels in the slag, and increases the silicon content in Liquid#1 and the alumina amount within the slag proportionally. This trend last until

1862.69°C where Fe-liq is fully consumed (Figure 34). These findings highlight how remaining aluminum promotes silica reduction, changing the chemistry of the molten and slag phases in the system, to a low extent in this specific case (Figure 35).

Constituents	Amount (g)	Temperature (°C)	Stream
SiO_2	20.04	1500	1
TiO_2	0.66	1500	1
Al_2O_3	10.29	1500	1
Fe_2O_3	8.17	1500	1
MnO	1.65	1500	1
MgO	11.24	1500	1
CaO	44.96	1500	1
Na2O	0.07	1500	1
K_2O	0.01	1500	1
P_2O_5	0.04	1500	1
Cr_2O_3	3.231	1500	1
Al	35.5	25	2
Fe	64	25	2
SiO_2	30.89	25	2

Table 14 inputs used for thermodynamic simulation.

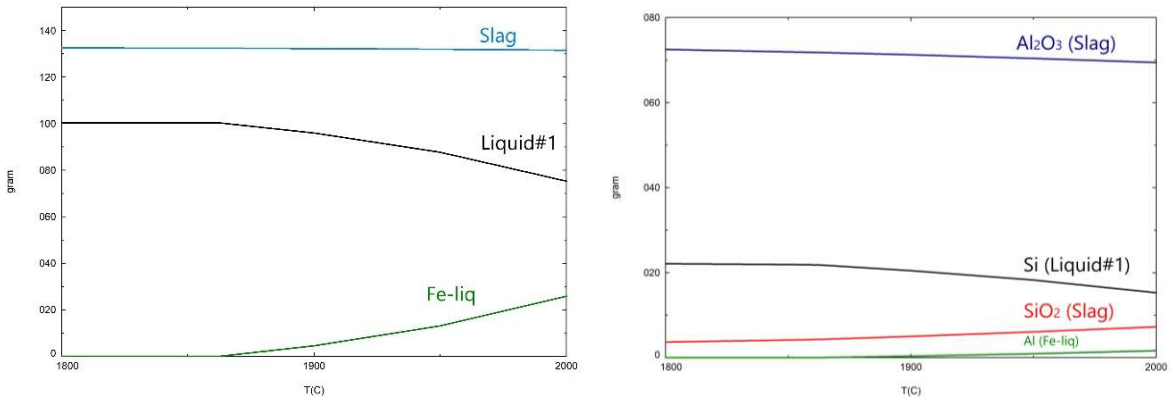

Figure 34 A general view of system interaction between phases Fe-liq, Liquid#1 and slag (left); a more detailed analysis of the same phases across a wider temperature range (right).

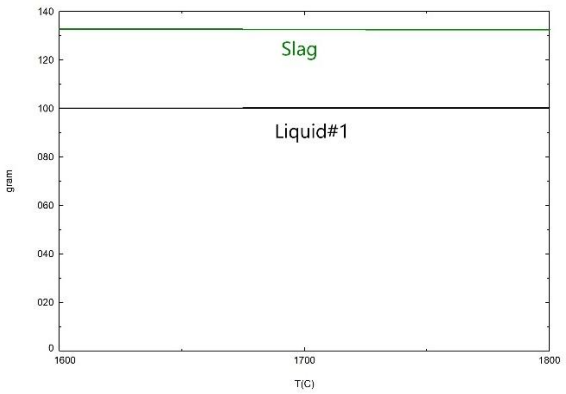

PHASE: LIQUID#1	gram		WEIGTH %	
Al	1.4406E+00	- 1.4646E+00	1.4403E+00	- 1.4551E+00
Cr	2.2105E+00	+ 8.7700E-04	2.2100E+00	+ 7.9160E-03
Fe	7.1714E+01	+ 1.0400E-03	7.1699E+01	+ 2.2950E-01
Mn	1.2769E+00	+ 4.9980E-03	1.2766E+00	+ 9.0490E-03
Si	2.2957E+01	+ 1.1394E+00	2.2952E+01	+ 1.2086E+00
Ti	3.5845E-01	+ 5.2688E-02	3.5837E-01	+ 5.3651E-02
TOTAL :	1.0002E+02	- 3.1980E-01	1.0000E+00	-

PHASE: LIQUID#2	gram		WEIGTH %	
Al	0.0000E+00	+ 0.0000E+00	1.4403E+00	+ 1.3634E+00
Cr	0.0000E+00	+ 0.0000E+00	2.2100E+00	+ 2.1161E+00
Fe	0.0000E+00	+ 0.0000E+00	7.1699E+01	- 2.0355E+01
Mn	0.0000E+00	+ 0.0000E+00	1.2766E+00	+ 1.2469E+00
Si	0.0000E+00	+ 0.0000E+00	2.2952E+01	+ 4.1952E+00
Ti	0.0000E+00	+ 0.0000E+00	3.5837E-01	+ 3.5569E-01
TOTAL :	0.0000E+00	+ 0.0000E+00	1.0000E+00	-

PHASE: Slag-liq#1	gram		WEIGTH %	
Al2O3	7.4568E+01	+ 2.7600E+00	5.6181E+01	+ 1.9488E+00
SiO2	1.8179E+00	- 2.4375E+00	1.3696E+00	- 1.8442E+00
CaO	4.4924E+01	+ 4.3150E-02	3.3846E+01	- 4.9130E-02
MgO	1.1207E+01	+ 3.5670E-02	8.4433E+00	+ 6.5490E-03
TOTAL :	1.3273E+02	+ 3.1980E-01	1.0000E+00	-

Figure 35 Slag and Liquid interaction (left); XML window featuring the mass balance of compound exchanges between slag and Liquid#1 from 1800 to 1500°C (right).

Beginning around 1600°C, the slag transforms into a number of different phases. As seen in Figure 36, Ti-Spinel#1 forms at around 1568.78°C. Following this transformation, calcium aluminate begins to occur at around 1419.92°C. Finally, around 1336.23°C, the remaining slag precipitates as $Ca_3MgAl_4O_{10}$.

Figure 36 shows how phase emergence corresponds with slag mass drops. In particular, the formation of and Ti-Spinel#1 and calcium aluminate align with the first and second drops in slag mass line, respectively. The most significant slag mass fall however, is mostly linked to formation of $Ca_3MgAl_4O_{10}$. additionally, a drop in the concentration of Ti-Spinel in the same temperature approves that this phase helps the slag in the precipitating the $Ca_3MgAl_4O_{10}$ phase. Figure 36 shows a more detailed illustration of these phenomenon. The appearance of Ti-Spinel#1, a phase primarily consisting of magnesium and alumina, aligns with the predicted decrease in MgO and alumina in the slag. Following a further drop in the concentration of alumina and CaO, $CaAl_2O_4$ is formed. The slag stops contributing to the system at about 1300°C, when it has completely consumed.

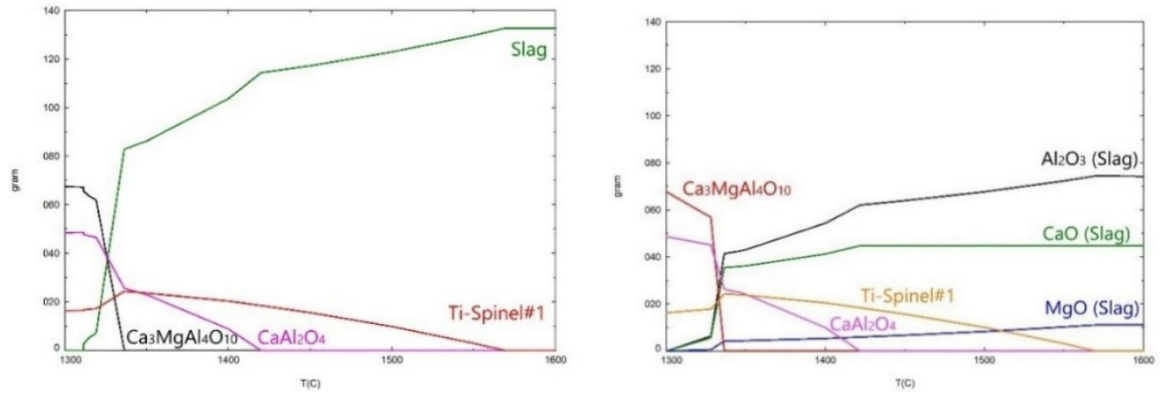

Figure 36 Transformation of slag into various phases (left); A more detailed view of compounds consumed for each phase formation (right).

Focusing on the metallic phases, the Liquid#1 presents good stability until approximately 1300°C. However, at the temperature 1284.3°C, the Liquid#1 phase converts into the Me_1Si_1 phase. Ultimately, the emergence of the M_5Si_3 and BCC2#1 phases represents the endpoint of the Liquid#1 interaction (1043.9°C) and transformations (Figure 37).

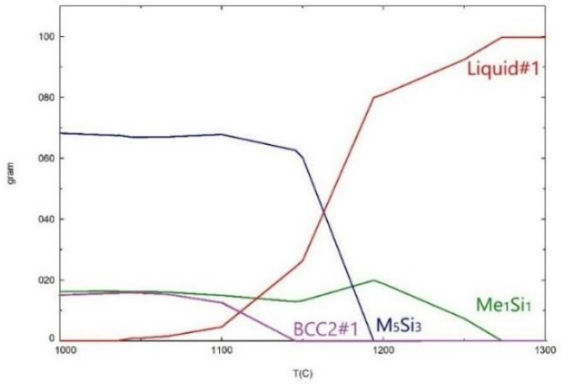

Figure 37 Emerged phase during Liquid#1 cooldown.

By examining the slag composition provided by the software on the ternary and quaternary phase diagram, it can be seen that on both diagrams the composition coordination falls within the desired calcium aluminate region (Figure 38). Additionally, the composition breakdown of the slag is provided in Table 15. According to reaction mass balance this process releases 38.87 joule per gram, or 10.8kWh/ton.

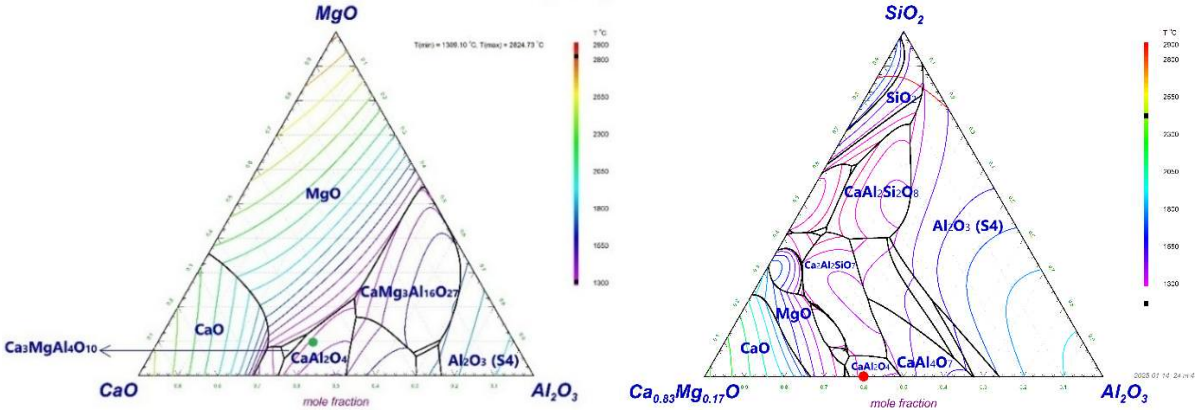

Figure 38 Ternary phase diagram and the marked point corresponding to slag composition (left); quaternary phase diagram of the same slag with marked point representing the composition (right).

SiO_2	1.37
TiO_2	-
Al_2O_3	56.18
Fe_2O_3	-
MnO	-
MgO	8.44
CaO	33.84
Na_2O	0.01
K_2O	-
P_2O_5	-

Table 15 composition of slag within slag-forming temperatures

The ferroalloy product with composition shown in Table 16 was obtained.

Element	Wt.%
Al	0.48
Cr	2.25
Fe	7.26
Mn	1.30
Si	24.22

Table 16 Metallic liquid (Liquid#1) composition.

Different charge states of iron were detected in the samples and their occurrence varied. In Slag_E, the metallic iron appeared as α-Fe, Pure iron in its zero-valent metallic state (Fe^0), while the iron oxides with 3^+ and 2^+ charges were stabilized as enstatite $(Mg,Fe)SiO_3$, magnetite (Fe_3O_4) and wüstite (FeO)[20]. On the other hand, Slag_R represented a complete reduction of the iron oxide, where only metallic iron was detected in the form of α-Fe, cementite, iron carbide(FeC_3), and austenite[21].

Silicon was still detected in its oxidized state in Slag_E. The majority of this oxidized silicon crystallized as larnite (β-Ca_2SiO_4), gehlenite ($Ca_2Al_2SiO_7$), and enstatite [$(Mg,Fe)SiO_3$].

Oxidized silicon content was also found in the Slag_R composition and they crystallized as the same phases that were in previous sample, but since there were no iron oxides, enstatite phases were not formed, but γ-Ca_2SiO_4 (calcium Olivine / γ-

[20] Magnetite with chemical composition of $Fe^{2+}(Fe^{3+})_2(O^{2-})_4$,contains both ferrous (divalent, partially reduce) and ferric (trivalent, non-reduced) iron, suggesting crystallization in an environment containing intermediate levels of oxygen. Wüstite, $Fe^{2+}O$, where iron is mainly in the +2 state, forms when iron is partially reduced from Fe^{3+} to Fe^{2+} but has not progressed to pure metallic Fe. Enstatite, commonly known as ($MgSiO_3$) but can incorporate Fe^{2+} due to similar charge and size, leading to $(Mg,Fe)SiO_3$.

[21] Typically described as face-centered cubic (FCC) iron, often alloyed with nickel, chromium, or other metals in steelmaking contexts. Austenite arises when these alloying elements stabilize the FCC structure. It can persist in certain micro-regions where the temperature or local chemistry holds it in the γ phase.

Belite) was seen instead. Partial fusion increased the proportion of Mayenite ($12CaO \cdot 7Al_2O_3$) in both samples. The results can be seen in Figure 39.

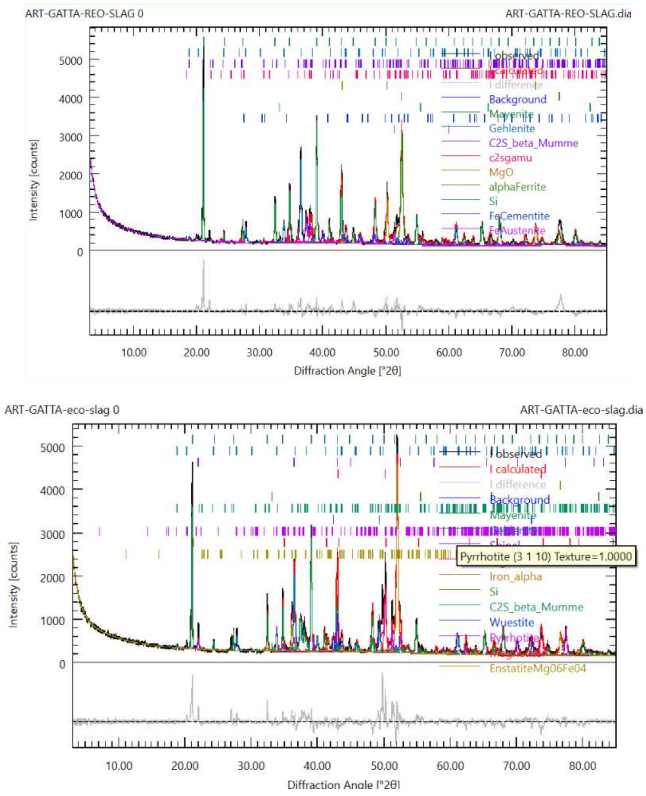

Figure 39 XRD analysis of Slag_R residual slag (top); Slag_E residual Slag (bottom).

Results from XRF analysis revels the compositional characteristics of the residual slags of the sample, confirming an incomplete reduction due to high levels of oxides present in the test sample (Table 17).

%Ox	Slag_E	Slag_R
SiO_2	32.02	36.20
TiO_2	0.24	0.16
Al_2O_3	22.19	20.71
Fe_2O_3	17.97	11.01
MnO	0.46	0.16
MgO	5.50	4.52
CaO	20.49	26.41
Na_2O	0.23	0.21
K_2O	0.03	0.01
P_2O_5	0.02	0.04

Table 17 XRF results

The impact of incomplete reduction is also clear in the metallic fraction evaluated via SEM–EDS. The ferroalloy component formed from Slag_E is mostly made of iron, with trace amounts of silicon, aluminum, and chromium, as seen in Figure 40 and Table 18. This composition differs significantly from the alloy that thermodynamic calculations predicted (Table 18 vs. Table 13), indicating that silicon was unable to fully incorporate into the alloy phase due to inadequate melting or non-reducing environment.

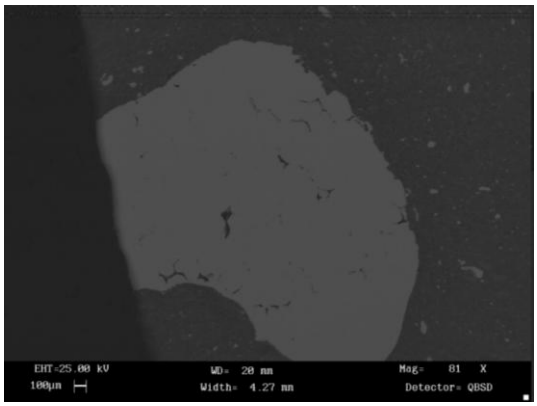

Figure 40 Slag_E ferroalloy sample extended view.

Element	Wt.%	At.%
Al	3.96	7.32
Si	7.72	13.70
Cr	1.55	1.48
Fe	86.77	77.49

Table 18 Quantitative analysis of ferroalloy form Slag_E

In case of ferroalloy obtained from Slag_R sample, the same trend of insufficient reducing atmosphere resulted iron as the major constituent, along with unreacted aluminum and traces of silicon is apparent (Table 19 and Figure 41). Magnifying into the sample was done to have a closer evaluation of the ferroalloy, however, no major difference was found in terms of composition as illustrated in Figure 42 and Table 20.

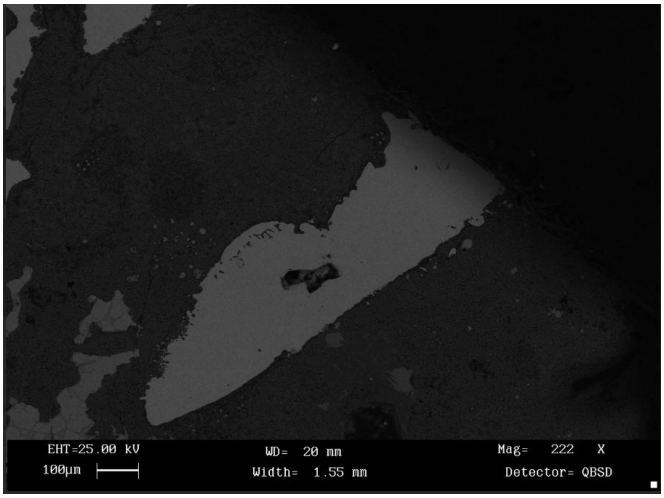

Figure 41 Slag_R ferroalloy extended view.

Element	Wt.%	At.%
Al	3.69	7.00
Si	5.18	9.45
Fe	91.13	83.55

Table 19 Quantitative analysis of ferroalloy form Slag_E

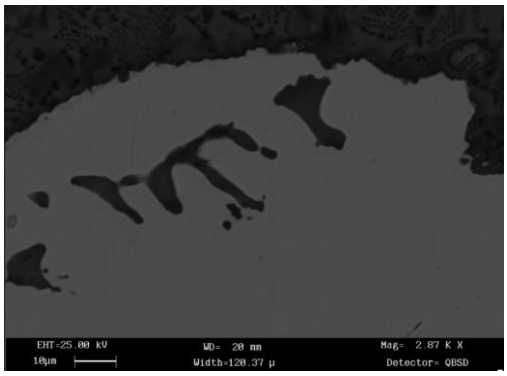

Figure 42 zoomed in view of Slag_R ferroalloy

Element	Wt.%	At.%
Al	1.80	3.43
Si	6.69	12.26
Fe	91.51	84.31

Table 20 Quantitative analysis of ferroalloy form Slag_R.

Higher-magnification SEM-EDS scans exhibited notable compositional changes within the ferroalloy microstructure. Figure 43 shows how zooming in on specific areas showed regional changes in elemental composition. For example, regions 1 and 2 had around 60 wt.% iron, 30% aluminum, and 10% silicon, while area 3 had almost equal amounts of iron and aluminum and little to no silicon. This magnified examination highlights how different elements concentrations can be found in micro-regions even

within a single alloy sample. This is probably due to insufficient mixing during solidification or localized reaction conditions.

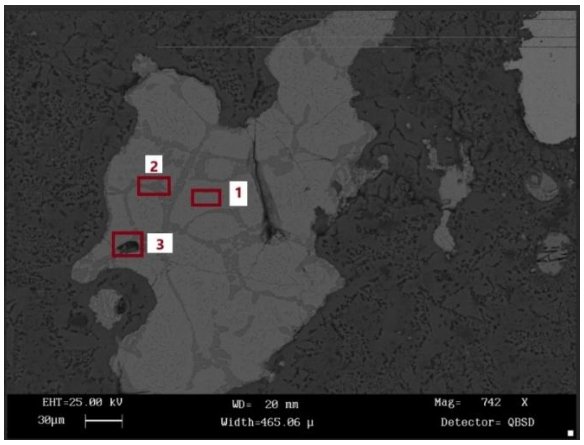

Figure 43 Magnification of Slag_R ferroalloy.

4 Discussions

Several iron-silicon compounds (silicides) can be found in the binary system Fe-Si under equilibrium conditions at different temperatures. They include FeSi, $FeSi_2$, Fe_3Si_7, Fe_5Si_3, Fe_2Si, and solid solutions based on an iron matrix (FCC or BCC), which precipitate after solidification (Stanisław et al., 2019). In other words, as silicon is introduced into iron crystals, the resulting phases shift in response to the silicon weight percentage. When the silicon content rises, the lattice evolves into a more ordered arrangement, moving from an FCC structure to intermetallic compounds like FeSi or $FeSi_2$ (Edmund et al., 2019). Sometimes, ferrosilicon alloys used in industry also contain small levels of impurities such as aluminum, calcium, magnesium, manganese, tin, phosphate, or sulfur. These impurities may appear as intermetallic and non-metallic compounds in a finished alloy. Their fractions are determined by the physicochemical reactions and raw material quality during production. Ferrosilicon should thus be regarded as a multicomponent system (Machulec & Bialik, 2016).

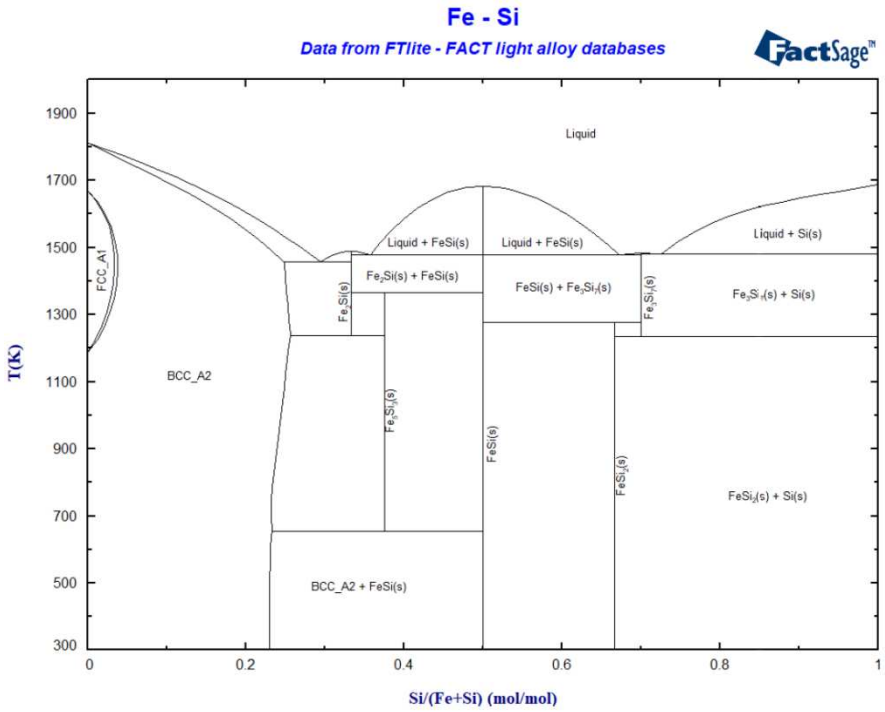

Figure 44 Iron-silicon phase diagram with molar fraction of Si vs. temperature (K), makes a path for analyzing the cooldown path and phase formation with respect to temperature and alloy composition (Stanisław et al., 2019).

By following a cooldown path on the phase diagram based on the composition of Liquid#1, the development of these intermetallic phases was also observed in the results of the thermodynamic simulations on both slag samples, confirming that silicon has effectively been embedded in the iron lattice. An iron-silicon phase diagram illustrates that a ferrosilicon composition with approximately 21 percent silicon is at a eutectic point, with a melting point of about 1212°C. The alloy yielded from the Slag_R sample in this study, on the other hand, had a slightly higher melting point of 1306°C and contained about 24% silicon. While it would have been possible to further lower the melting point by reducing the silicon content, maintaining a concentration of roughly 25 wt.% was necessary to comply with ISO standard requirements. Despite this drawback, the ferrosilicon derived from Slag_R can be traded commercially because it satisfies ISO requirements and maintains a low enough melting point.

The ferrosilicon produced by Slag_E has a low melting point of 1284°C and an acceptable silicon concentration of about 25 wt.%. However, the alloy is not eligible for commercial sales since it goes against ISO criteria due to its significant amounts of impurities, such as manganese and chromium (Table 16). These impurities are a result of the high levels of chromium and manganese oxide present in the slag sample, which reflect the approach that the company has taken in their its refining. The

accumulation of these impurities is inevitable within the molten phase, but considering the known composition, this alloy can be employed internally within the producing plant, as the impurities may serve as valuable alloying agents in later steel making operations (Figure 45).

By using iron and aluminum scrap as essential inputs, the economic viability of the process is greatly increased. Because these materials are significantly less expensive than their virgin counterparts, the total cost of raw materials is decreased. This approach may increase the possibility of greater revenue due to reduced input costs, but it also presents potential uncertainty in purity, which may require additional sorting or refining to maintain alloy quality and meet ISO specifications. Overall, this method provides a viable and cost-effective option for generating ferrosilicon while optimizing resource use and reducing financial burden.

Although effective optimization resulted in a calcium aluminate-based slag, impurities triggered the development of Ti-spinel and calcium-magnesium aluminate (CMA) during the cooldown. These spinel phases most likely formed when trace elements altered the ternary system's phase stability boundaries. Additionally, their existence does not necessarily prevent the use of the slag in cement manufacturing, because CMA and spinel-related phases can be converted back into calcium aluminate through sintering if the process requirements and overall economic feasibility justify it

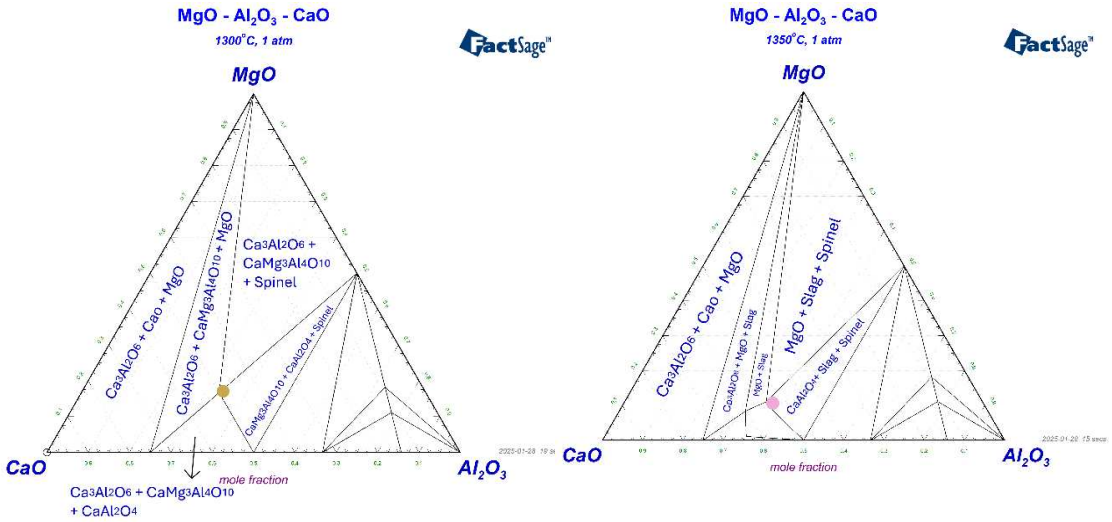

Figure 45 Phase diagrams in single temperature, aligns with the results of simulations in terms of spinel phases appearance.

Further moving the slag composition toward higher calcium aluminate phases—and thereby lowering calcium consumption via spinel formation—could have been achieved by increasing aluminum input. However, such actions were considered

impracticable as the possible advantages were not justified by the high cost of aluminum in comparison to bauxite (used for conventional calcium aluminate material making) and the risk of process instability. However, sufficient amounts of calcium aluminate phases are still present in the resulting residual slag to make it a suitable partial substitute for traditional CA materials, especially in refractory applications or any system that can benefit from the presence of CMA. This partial substitution lowers the energy demands of traditional techniques of producing calcium aluminate and minimizes the need for extracting virgin minerals.

In case of the practical experiment, the result from the spectroscopy analysis revealed a mixture of different oxidation states of iron within the residual slag. This situation indicates that iron oxides underwent partial and incomplete reduction; certain furnace zones must have provided sufficiently reducing conditions to produce α-Fe, while other areas retained Fe in higher oxidation states, thereby stabilizing the oxide and silicate phases. The emergence of aluminosilicates intermediates indicates that the furnace conditions neither allowed silica to form metallic silicon nor facilitated the path towards simpler calcium aluminates phases which can be a cause of the cooling kinetics or the local crystallization pathways that the samples took.

While some iron reached metallic form (α-Fe), the alloy still contains aluminum and lacks silicon, indicating that neither element was totally reduced or evenly distributed. This suggests that cooling and solidification occurred under localized reaction conditions. Thus, the alloy's composition revealed by SEM analysis represents the incomplete reaction pathways in the residual slag, demonstrating that furnace conditions, quick cooling, and partial fusion affected metal and slag compositions. Overall, these results illustrate how real furnace operations can deviate from theoretical simulations and showcases the importance of proper process design and optimization for minimizing these deviations.

This research demonstrates the concept of industrial symbiosis by converting ladle furnace slag into ferrosilicon and calcium aluminate residues that can be commercially traded. It highlights how waste from one industry can serve as a resource for another. The steel industry, for example, generates slag containing oxides that can be converted into valuable metals; in contrast, the aluminum industry provides waste or secondary material that supports this reduction process at a significantly lower energy cost than virgin aluminum. Lastly, the process produces an alloy commonly used in steelmaking for deoxidation, impurity removal, and as an alloying agent. Meanwhile,

the calcium aluminate-based slag formed during this process can be used to produce high-alumina cements, replacing the energy-intensive raw materials traditionally used in this sector with a more sustainable feedstock, thus reinforcing the circular economy by repurposing waste.

This integrated flow of raw materials and byproducts exemplifies a circular economy perspective. Plants can use the hidden value of slag instead of disposing of it, which reduces the strain on landfills and the need to harvest new minerals like quartz and bauxite. Utilizing aluminum and iron waste helps manufacturers reduce their carbon footprint and operational costs, as recycling these metals requires less energy than producing them from raw materials. These closed-loop material cycles enhance the resilience and competitiveness of each industry while minimizing their environmental impact.

Collectively, these synergies demonstrate a shift from traditional linear 'take-make-dispose' models to more circular ones, enabling resource sharing, waste reduction, and more sustainable operations through the utilization of secondary materials across several industries. Through such industrial collaboration, the steel, aluminum, and silicon industries can collectively reduce raw material consumption and greenhouse gas emissions while promoting more responsible growth, demonstrating that economic viability and sustainability can coexist.

Conclusion

This work proves that steelmaking slag can be a viable feedstock for ferrosilicon production if the reaction route is properly controlled and guided by thermodynamic simulations and phase diagram analysis. The resulting alloy meets ISO standards, and the residual slag , despite some inevitable deviation from the ideal calcium aluminate, offers sufficient calcium aluminate phases to be useful in cement applications. Conducting a multi-stage simulation test, including the trace impurities (embedded in the materials or introduced during the process depending on the equipment) may result in better prediction of the process outcome since undefined impurities can change the stability range of compounds. These results illustrate the practicality of the notion of industrial symbiosis, in which waste products from one metalworking process are directly fed into another, thus decreasing energy requirements and material waste. Although incomplete fusion and partial reactions occurred during the furnace trial,

more precise process design, better temperature management, more cooling control, and enhanced stirring or mixing systems can help overcome these obstacles. This aluminothermic method ultimately demonstrates a chance to promote circular economy concepts in metallurgy by turning high-volume slag into a useful iron-silicon alloy and a useful by-product for other industrial applications.

Acknowledgement

I am deeply grateful to Professor Katya Brunelli for her invaluable guidance throughout this project. Her insightful supervision shaped every phase of my research. I would also like to thank Opigeo SRL for providing the slag samples and granting me access to both the software and the furnace. I am very much grateful to Professor Bellotto for generously offering his expertise and time, especially during pivotal moments of this work.

A very special thanks goes to Dr. Filippo—holder of the world record in fastest email responses—without whose tutorials and bright ideas, I would have been lost in navigating the software, interpretating the results and reporting them; trust me, Fillipo, your promptness saved this entire project!

I also want to express my heartfelt appreciation to my family, whose belief in me made it possible to join the University of Padova and pursue this endeavor. I will never forget the early days in Padova when Mohammad Hemasian, Saba Sajedi, and Alem Khodadi made sure I never felt alone or adrift; your friendship meant more than words can say. And to my dear friend Erfan Efati, thanks for the endless meetups, calls and chats, and more importantly, the much-needed beers—they truly kept us both motivated!

lastly, I would like to mention, Erfan Valizadeh, for all the calls he made to make sure I am doing well, our long history can't be summarized within few words.

To all others who contributed in ways both large and small, I hope my future successes will repay the trust and faith you have shown in me. Thank you for everything.

References

Abd Mutalib, Muhazri, Rahman, M., Othman, M. H., Ismail, A., & Jaafar, J. (2017). Scanning Electron Microscopy (SEM) and EnergyDispersive XRay (EDX) Spectroscopy. In *Membrane Characterization* (pp. 161–179). https://doi.org/10.1016/B9780444637765.000097

Abukersh, S. A., & Fairfield, C. A. (2011). Recycled aggregate concrete produced with red granite dust as a partial cement replacement. *Construction and Building Materials*, *25*(10), 4088–4094. https://doi.org/10.1016/j.conbuildmat.2011.04.047

Ahindra Ghosh, & Amit Chatterjee. (2008). *Ironmaking and steelmaking : Theory and practice*. Prentice-Hall of India.

AISE Steel Foundation. (1999). *The making, shaping, and treating of steel: Ironmaking volume* (W. D. H. (Ed.), Ed.; 11th ed., pp. 547–642). AISE Steel Foundation. https://books.google.it/books?id=875TAAAAMAAJ

Ali, A., & Akhtar, M. Asim. (2015). *Comparative Study on High Temperature Oxidation Behavior of Austenitic Stainless Steels in Different Environments*. https://doi.org/10.13140/RG.2.1.2677.9042

Andersen, V. (2023). Flue Gas Recirculation for the Silicon Process. *Handle.net*. https://doi.org/978-82-326-5299-0

Babich, A., & Senk, D. (2013). Biomass use in the steel industry: Back to the future? *Stahl Und Eisen*, *133*(5), 57–67.

Bhagyadhar Bhoi, Murthy, R., Datta, P., Rajeev, & Jouhari, A. K. (1997). *Studies on aluminothermic reduction of manganese ore for ferro-manganese making*. https://api.semanticscholar.org/CorpusID:55844486

Brandt, D. A., & Warner, J. C. (1999). *Metallurgy Fundamentals* (3rd ed.). Goodheart-Wilcox Publisher.

Brouwer, P. (2003). *Theory of XRF : getting acquainted with the principles* (3rd ed., pp. 9–57). Panalytical.

Brown, T., & Fennell, P. S. (2012). Reducing CO2 emissions from heavy industry: a review of technologies and considerations for policy makers. *Grantham Institute for Climate Change, Imperial College London*. https://api.semanticscholar.org/CorpusID:54869968

Chen, J., & Wei, S. (2016). Engineering properties and performance of asphalt mixtures incorporating steel slag. *Construction and Building Materials*, *128*, 148–153. https://doi.org/10.1016/j.conbuildmat.2016.10.027

Choudhary, J., Kumar, B., & Gupta, A. (2020). Utilization of solid waste materials as alternative fillers in asphalt mixes: A review. *Construction and Building Materials*, *234*, 117271.

https://doi.org/10.1016/j.conbuildmat.2019.117271

Crawford, J. (2015). *GLOBAL SUSTAINABLE DEVELOPMENT REPORT 2015 EDITION ADVANCE UNEDITED VERSION*. https://sustainabledevelopment.un.org/content/documents/1758GSDR%202015%20Advance%20Unedited%20Version.pdf

Cw Group. (2023). *Global Calcium Aluminate Cement Market Report and Forecast – 2023*. Cwgrp.com. https://cwgrp.com/cemweek-reports/product/286-global-calcium-aluminate-cement-market-report-and-forecast-%e2%80%93-2023

Dávila, O. F., Torres, J. T., & Valdes, A. F. (2019). Effect of Mg Concentration on the Aluminothermic Reduction of Mn2O3 Particles Obtained from Cathodes of Discharged Alkaline Batteries: Mathematical Modeling and Experimental Results. *Metals*, *9*(1). https://doi.org/10.3390/met9010049

Edmund, E., Antonangeli, D., Decremps, F., Morard, G., Ayrinhac, S., Gauthier, M., Boulard, E., Mezouar, M., Hanfland, M., & Guignot, N. (2019). Structure and elasticity of cubic Fe-Si alloys at high pressures. *Phys. Rev. B*, *100*(13), 134105. https://doi.org/10.1103/PhysRevB.100.134105

Eissa, M., & El-Farmawy, H. (2012). Carbothermic smelting of high carbon ferrochromium alloy from low and high grade chromite ores. *Ironmaking & Steelmaking*, *39*(1), 31–37. https://doi.org/10.1179/1743281211y.0000000047

Elkam . (2018). *Annual report 2018*. https://www.elkem.com/globalassets/corporate/documents/elkem-annual-report-2018-print-and-tablet2.pdf

Eric, R. H. (2014). *Chapter 1.10 - production of ferroalloys* (S. Seetharaman, Ed.; pp. 477–532). Elsevier. https://doi.org/10.1016/B978-0-08-096988-6.00005-5

EUROPEAN AGGREGATES ASSOCIATION. (2017). *EUROPEAN AGGREGATES ASSOCIATION A Sustainable Industry for a Sustainable Europe*. https://www.aniet.pt/fotos/editor2/uepg_annual_review_2017-2018_003_.pdf

Fathi , H. (2018). *Metallothermic Reactions - Past, Present and Future Res Rep Metals 2:1*. https://www.scitechnol.com/peer-review/metallothermic-reactions--past-present-and-future-lUnd.php?article_id=7214

Felipe, L., Daniel Fernández González, & Verdeja, I. (2021). *Operations and Basic Processes in Steelmaking*. Springer Nature.

Guo, Z., Jianying, G., & Feifang, G. (2021). China's Refractories, Vol.30, No.1. *China's Refractories*, *30*.

Han, B., Yu, X., & Ou, J. (2014). *Self-sensing concrete in smart structures*.

Harrington, G. F., & Santiso, J. (2021). BacktoBasics tutorial: Xray diffraction of thin films. *Journal of Electroceramics*, *47*(4), 141–163. https://doi.org/10.1007/s10832021002636

Henriques, J., Castro, P. M., Dias, R., Magalhães, B., & Estrela, M. (2023). Potential industrial synergies in the steelmaking and metal-processing industry: By-products valorization and associated technological processes. *Sustainability*, *15*, 21. https://doi.org/10.3390/su152115323

Hoover, H., Bell, R., & Rippy, K. (2024). Emerging Technologies for Decarbonizing Silicon Production. *Journal of Sustainable Metallurgy*, *10*(4), 1921–1932. https://doi.org/10.1007/s40831-024-00913-3

IEA. (2020, October). *Iron and steel technology roadmap–analysis*. IEA. https://www.iea.org/reports/iron-and-steel-technology-roadmap

J.J., P. (1999). *The making, shaping, and treating of steel: Ironmaking volume* (11th ed.). AISE Steel Foundation. https://books.google.it/books?id=875TAAAAMAAJ

Juckes, L. M. (2003). The volume stability of modern steelmaking slags. *Mineral Processing and Extractive Metallurgy*, *112*, 3. https://doi.org/10.1179/037195503225003708

Kaffash, H., Surup, Gerrit Ralf, & Tangstad, M. (2021). Densification of biocarbon and its effect on CO2 reactivity. *Processes*, *9*, 2. https://doi.org/10.3390/pr9020193

Kavussi, A., & Jalili, Q. M. (2014). Fatigue characterization of asphalt mixes containing electric arc furnace (EAF) steel slag subjected to long term aging. *Construction and Building Materials*, *72*, 158–166. https://doi.org/10.1016/j.conbuildmat.2014.08.052

Kero, I., Grådahl, S., & Tranell, G. (2017). Airborne Emissions from Si/FeSi Production. *JOM*, *69*(2), 365–380. https://doi.org/10.1007/s118370162149x

Kero, I., Osen, K., & Dalaker, H. (2022). Technologies with potential for climate neutral silicon production. *SSRN Electronic Journal*. https://doi.org/10.2139/ssrn.4121151

Kudyba, A., Akhtar, S., Johansen, I., & Safarian, J. (2021). Aluminothermic Reduction of Manganese

Oxide from Selected MnOContaining Slags. *Materials*, *14*(2). https://doi.org/10.3390/ma14020356

Lachmund, H., & Xie, Y. (2001). Thermodynamic and kinetic aspects of the desulphurisation reaction in secondary metallurgy. *Steel Research*, *72*, 452–459. https://doi.org/10.1002/srin.200100151

Lee, J., Choi, J., Yuan, T., Yoon, Y., & Mitchell, D. (2019). Comparing Properties of Concrete Containing Electric Arc Furnace Slag and Granulated Blast Furnace Slag. *Materials*, *12*(9). https://doi.org/10.3390/ma12091371

Levi, E., Sgarbi, S., & Piana, E. A. (2021). Acoustic Characterization of Some Steel Industry Waste Materials. *Applied Sciences*, *11*(13), 5924–5924. https://doi.org/10.3390/app11135924

Li, F., Tangstad, M., & Ringdalen, E. (2018). Carbothermal Reduction of Quartz and Carbon Pellets at Elevated Temperatures. *Metallurgical and Materials Transactions B*, *49*(3), 1078–1088. https://doi.org/10.1007/s116630181195x

Liu, J., Chen, Z., Ma, W., Wei, K., & Ding, W. (2018). Application of a Waste Carbon Material as the Carbonaceous Reductant During Silicon Production. *Silicon*, *10*(6), 2409–2417. https://doi.org/10.1007/s1263301897729

Lombardi, D., & Laybourn, P. (2012). Redefining Industrial Symbiosis. *Journal of Industrial EcologyJ IND ECOL*, *16*. https://doi.org/10.1111/j.15309290.2011.00444.x

M, W. B., H, Z. T., S, F. C., R, M. N., & Godinho, M. (2013). Aluminothermic reduction of Cr2O3 contained in the ash of thermally treated leather waste. *Brazilian Journal of Chemical Engineering*, *30*.

Machulec, B., & Bialik, W. (2016). Comparison the PhysicoChemical Model of Ferrosilicon Smelting Process with Results Observations of the Process under the Industrial Conditions. *Archives of Metallurgy and Materials*, *61*, 265–270. https://doi.org/10.1515/amm20160050

Maghool, F., Arulrajah, A., Du, Y., Horpibulsuk, S., & Chinkulkijniwat, A. (2017). Environmental impacts of utilizing waste steel slag aggregates as recycled road construction materials. *Clean Technologies and Environmental Policy*, *19*(4), 949–958. https://doi.org/10.1007/s1009801612896

Monsen, B., Grønli, M., Nygaard, L., & Tveit, H. (2001). The Use of Biocarbon in Norwegian Ferroalloy Production. *INFACON*, *9*, 268–276.

Mousa, E., Wang, C., Riesbeck, J., & Larsson, M. (2016). Biomass applications in iron and steel industry: An overview of challenges and opportunities. *Renewable and Sustainable Energy Reviews*, *65*, 1247–1266. https://doi.org/10.1016/j.rser.2016.07.061

Nick, S., Leinonen, V., Mäyrä, J., & Björkvall, J. (2021). Towards greener industry: Modelling of slag heat recovery. *Metals*, *11*, 7. https://doi.org/10.3390/met11071144

Nygård, H., Meyer, J., Felice, D., Eldrup, N., Haug, A., & Olsen, E. (2019). *Technoeconomic study of the ccms technology for CO2 capture from ferrosilicon production*.

Ochoa ,R, Flores ,A, Torres ,J, Guía ,J, & Muñiz ,R. (2016). Kinetic study on the metallothermic reduction of chromite ore using magnesium scrap. *Canadian Metallurgical Quarterly*, *55*(2), 210–220. https://doi.org/10.1080/00084433.2016.1146432

Pasetto, M., & Baldo, N. (2011). Mix design and performance analysis of asphalt concretes with electric arc furnace slag. *Construction and Building Materials*, *25*(8), 3458–3468. https://doi.org/10.1016/j.conbuildmat.2011.03.037

Piemonti, A., Conforti, A., Cominoli, L., Sorlini, S., Luciano, A., & Plizzari, G. (2021). Use of iron and steel slags in concrete: State of the art and future perspectives. *Sustainability*, *13*, 2. https://doi.org/10.3390/su13020556

Remus, R., Aguado, M. M., Roudier, S., & Delgado, S. L. (2013, January 24). *Best Available Techniques (BAT) Reference Document:for:Iron and Steel Production:Industrial Emissions Directive 2010/75/EU:(Integrated Pollution Prevention and Control)*. JRC Publications Repository. https://publications.jrc.ec.europa.eu/repository/handle/JRC69967

Ren, Z., & Li, D. (2023). Application of Steel Slag as an Aggregate in Concrete Production: A Review. *Materials*, *16*(17). https://doi.org/10.3390/ma16175841

Saly, F., Guo, L., Ma, R., Gu, C., & Sun, W. (2018). Properties of Steel Slag and Stainless Steel Slag as Cement Replacement Materials: A Comparative Study. *Journal of Wuhan University of TechnologyMater. Sci. Ed.*, *33*(6), 1444–1451. https://doi.org/10.1007/s1159501819893

Schei, A., Tuset, J., & Tveit, H. (1998). *Production of high silicon alloys*.

Scrivener, K. L., Jean-Louis Cabiron, & Letourneux, R. (1999). High-performance concretes from calcium aluminate cements. *Cement and Concrete Research*, *29*, 8. https://doi.org/10.1016/S0008-8846(99)00103-9

Shen, D.-H., Wu, C.-M., & Du, J.-C. (2009). Laboratory investigation of basic oxygen furnace slag for

substitution of aggregate in porous asphalt mixture. *Construction and Building Materials*, *23*(1), 453–461. https://doi.org/10.1016/j.conbuildmat.2007.11.001

Shi, C. (2004). Steel Slag—Its production, processing, characteristics, and cementitious properties. *Journal of Materials in Civil Engineering*, *16*, 3. https://doi.org/10.1061/(ASCE)0899-1561(2004)16:3(230)

Singh, C. S., Singh, P. K., Kumar, K. P., & Randhawa, N. S. (2023). A Review on Environmental Concerns and Technological Innovations for the Valorization of Steel Industry Slag. *Mining, Metallurgy & Exploration*, *40*(6), 2059–2086. https://doi.org/10.1007/s4246102300886z

Stanisław, G., Wojciech, B., Bolesław, M., & Sławomir, K. (2019). *IRON AND STEELMAKING 2019 MODERN METALLURGY The XXVIII INTERNATIONAL SCIENTIFIC CONFERENCE Conference proceedings WELLNESS HOTEL CHOPOK, DEMÄNOVSKÁ DOLINA, LIPTOVSKÝ MIKULÁŠ, SLOVAKIA 23 rd to 25 th* (pp. 134–140). https://ohaz.umet.fmmr.tuke.sk/iasm2019/conference_proceedings.pdf

Sundholm , Valia , Kiessling , Richardson, Buss , Worberg, Schwarz, Baer, Calderon, & DiNitto R. (1999). Manufacture of metallurgical coke and recovery of coal chemicals. In W. D. H (Ed.), *The making, shaping, and treating of steel: Ironmaking volume* (11th ed., pp. 381–546). AISE Steel Foundation.

Tomažič, S., Škrjanc, I., Andonovski, G., & Logar, V. (2024). The Development of Simulation and Optimisation Tools with an Intuitive User Interface to Improve the Operation of Electric Arc Furnaces. *Machines*, *12*(8). https://doi.org/10.3390/machines12080508

Transactions and communications. (1944). *Journal of the Society of Chemical Industry*, *63*, 5. https://doi.org/10.1002/jctb.5000630501

United Nations. (2024). *Sustainable Development Goals*. United Nations Sustainable Development; United Nations. https://www.un.org/sustainabledevelopment/sustainable-development-goals/

Worldsteel Association. (2018). *#Steelfacts*. Worldsteel.org. https://worldsteel.org/about-steel/facts/steelfacts/

Wörtler, M., Löngen, H. B., Ghenda, J. T., Dahlmann , P., Schuler, F., Voigt, N., & Schmidt, T. (2015). Steel's contribution to a lowcarbon Europe 2050: Technical and economic analysis of the steel sector's CO2 abatement potential. *Iron and Steel Technology*, *12*, 62–72.

Xakalashe, B., & Tangstad, M. (2011). *Silicon processing: from quartz to crystalline silicon solar cells*.

Xing, Z., Lu, J., & Ji, X. (2018). A Brief Review of Metallothermic Reduction Reactions for Materials Preparation. *Small Methods*, *2*(12), 1800062. https://doi.org/10.1002/smtd.201800062

Yao, S., Wu, S., Song, B., Kou, M., Zhou, H., & Gu, K. (2018). Multi-objective optimization of cost saving and emission reduction in blast furnace ironmaking process. *Metals*, *8*, 12. https://doi.org/10.3390/met8120979

Yildirim, I. Z., & Prezzi, M. (2011). Chemical, mineralogical, and morphological properties of steel slag. *Advances in Civil Engineering*, *2011*, 1. https://doi.org/10.1155/2011/463638

Yu, Y., Li, B., Yun, C., Qi, F., & Liu, Z. (2021). Modeling on Reduction Reaction of Metal Oxides for Submerged Arc Furnace in Ferrochrome Pellets Smelting Process. *Metallurgical and Materials Transactions B*, *52*(6), 3907–3919. https://doi.org/10.1007/s11663021023045

Zapata, J. F., Azevedo, A., Fontes, C., Monteiro, S. N., & Colorado, H. A. (2022). Environmental impact and sustainability of calcium aluminate cements. *Sustainability*, *14*, 5. https://doi.org/10.3390/su14052751